

Channel Estimation in RIS-Assisted MIMO Systems Operating Under Imperfections

Paulo R. B. Gomes, Gilderlan T. de Araújo, Bruno Sokal, André L. F. de Almeida, *Senior Member, IEEE*, Behrooz Makki, *Senior Member, IEEE*, and Gábor Fodor, *Senior Member, IEEE*

Abstract—Reconfigurable intelligent surface (RIS) is a potential technology component of future wireless networks due to its capability of shaping the wireless environment. The promising gains of RIS-assisted multiple-input multiple-output (MIMO) systems in terms of extended coverage and enhanced capacity are, however, critically dependent on the accuracy of the channel state information. However, traditional channel estimation schemes are not applicable in RIS-assisted MIMO networks, since passive RISs typically lack the signal processing capabilities that are assumed by channel estimation algorithms. This becomes most problematic when physical imperfections or electronic impairments affect the RIS due to its exposition to different environmental effects or caused by hardware limitations from the circuitry. While these real-world effects are typically ignored in the literature, in this paper we propose efficient channel estimation schemes for RIS-assisted MIMO systems taking different imperfections into account. Specifically, we propose two sets of tensor-based algorithms, based on the parallel factor analysis decomposition schemes. First, by assuming a long-term model – in which the RIS imperfections, modeled as unknown phase shifts, are static within the channel coherence time – we formulate an iterative alternating least squares (ALS)-based algorithm for the joint estimation of the communication channels and the unknown phase deviations. Next, we develop the short-term imperfection model, which allows both amplitude and phase RIS imperfections to be non-static with respect to the channel coherence time. We propose two iterative ALS-based and closed-form higher order singular value decomposition-based algorithms for the joint estimation of the channels and the unknown impairments. Moreover, we analyze the identifiability and computational complexity of the proposed algorithms and study the effects of various imperfections on the channel estimation quality. Simulation results demonstrate the effectiveness of the proposed tensor-based algorithms in terms of estimation accuracy and computational complexity.

Index Terms—Alternating least squares (ALS), channel estimation, hardware impairments, higher-order singular value decomposition (HOSVD), imperfection detection, multiple input multiple output (MIMO), parallel factor analysis (PARAFAC), reconfigurable intelligent surface (RIS).

Paulo R. B. Gomes, Gilderlan T. de Araújo, Bruno Sokal, and André L. F. de Almeida are with the Wireless Telecom Research Group (GTEL), Department of Teleinformatics Engineering, Federal University of Ceará, Fortaleza-CE. E-mail: {paulo.gilderlan,brunosokal,andre}@gtel.ufc.br.

Behrooz Makki is with Ericsson Research, Göteborg, Sweden. E-mail: behrooz.makki@ericsson.com.

Gábor Fodor is with Ericsson Research and KTH Royal Institute of Technology, Stockholm, Sweden. E-mail: gabor.fodor@ericsson.com.

This work was supported by the Ericsson Research, Sweden, and Ericsson Innovation Center, Brazil, under UFC.48 Technical Cooperation Contract Ericsson/UFC. This study was financed in part by the Coordenação de Aperfeiçoamento de Pessoal de Nível Superior - Brasil (CAPES)-Finance Code 001, and CAPES/PRINT Proc. 88887.311965/2018-00. André L. F. de Almeida acknowledges CNPq for its financial support under the grant 312491/2020-4. Gábor Fodor was partially supported by the Digital Futures project PERCy.

Part of this work has been submitted for possible presentation in IEEE GLOBECOM 2022 [1].

I. INTRODUCTION

Wireless communications have become a necessity in our daily lives providing significant benefits to individuals, businesses and the society at large. The steadily increasing demands for ubiquitous wireless services drive the efforts by the research and standardization communities to improve coverage, system capacity as well as the reliability and quality of a growing number of applications [2], [3]. The continuous growth of the number of mobile subscriptions, devices and traffic increases the number of deployed infrastructure nodes, which makes capital and operational expenditures as well as energy consumption challenging for mobile network operators. [4]. Therefore, to guarantee green sustainable wireless networks, one needs to carefully take the energy consumption and the hardware costs into account [5], [6].

Thanks to the recent development of meta-materials, reconfigurable intelligent surface (RIS) has emerged as a potential technology applicable in future wireless networks through the novel *smart and programming environment* paradigm [7]. Unlike conventional networks, RIS-assisted networks enable the system to shape the wireless environment to be more suitable for wireless communication [8], [9]. In conventional networks, the wireless transmission medium is seen as an uncontrollable element in the system due to the randomness in the radio environment. Therefore, the propagation of electromagnetic waves through the wireless channel cannot be controlled after they are emitted from the transmitters and before they reach the receivers [10]. An RIS is a planar meta-surface that has a large number of low-cost passive reflecting elements with adjustable capability of the reflected signal parameters such as amplitude, phase, frequency and polarization. With a well-configured RIS, the propagation conditions are improved by controlling the scattering characteristics to create passive and active beamforming at the RIS and the wireless transceivers, respectively, to achieve high beamforming gains [11]. In addition, a passive RIS does not require active radio frequency chains for signal transmission, reception and processing, since it simply relies on passive signal reflection, which makes it a power-efficient and less-complexity technology [12]–[15].

Despite its potential benefits, the performance gains achieved in RIS-assisted systems are strongly dependent on, among others factors, the quality of the channel state information (CSI), where the channel between the wireless transceivers is effectively split into two-hop RIS-assisted channels. This is because CSI is required to jointly design the passive beamforming at the RIS and the active beamforming at the transceivers [16]. However, due to the passive nature of the RIS, channel estimation is not performed at the RIS but only on gNB or UE side.

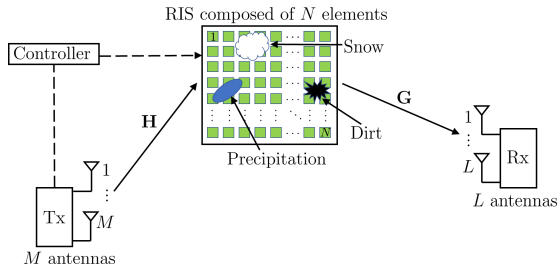


Fig. 1: An illustration of a RIS-assisted MIMO wireless communication system operating under imperfections.

Recognizing this issue, recent works propose different strategies to tackle the channel estimation problem in RIS-assisted wireless communications under various configurations (see, e.g., [17]–[19] and references therein). The most popular approach in the literature, known as the on/off method, consists of switching groups of RIS elements (or each individual element) to estimate the associated channel coefficients sequentially [20]. More specifically, each element of the cascaded channel is estimated at each time slot from pilots sent by the transmitter and reflected by the corresponding RIS element e.g., [21].

In the context of RIS-assisted multiple-input multiple-output (MIMO) systems, [22] proposes a two-stage algorithm including sparse matrix factorization and matrix completion to estimate the channels in massive array setups. In [23], the authors leverage compressed sensing (CS) and deep learning tools to reduce the training overhead. In a similar way, [24] also uses CS techniques and proposes a two-step iterative solution to solve the problem in a multi-user scenario. Then, [25] proposes an iterative method to estimate the channel parameters (angle of departure, angle of arrival and propagation path gains) in RIS-assisted millimeter wave (mmWave) MIMO systems, resulting in limited training overhead.

Over the past two decades, tensor algebra and higher-order tensor decompositions have been successfully applied to signal modeling and processing in wireless communications. Tensor-based signal processing exploits the intrinsic multidimensional structure of wireless channels and signals to achieve an improved estimation accuracy under more relaxed and flexible system parameter settings, compared to conventional matrix-based approaches [26]–[28].

Recently, tensor approaches have been proposed in the context of RIS-assisted wireless communications. Particularly, [29] capitalizes on the parallel factor (PARAFAC) decomposition to formulate an efficient iterative algorithm based on the alternating least squares (ALS) concept to solve the channel estimation problem in the downlink of a multi-user multiple input single output (MISO) network. Also, in [30] and [31], the authors develop simple iterative and closed-form channel estimation algorithms based on a PARAFAC modeling of the single-user MIMO scenario.

The main motivation for RIS is complexity/energy reduction, otherwise integrated access and backhaul (IAB) nodes, relays, and/or repeaters may be alternatives. Then, complexity reduction may affect the hardware capability and, consequently, its performance. Therefore, to have a realistic view on the performance and usefulness of RIS, one needs to carefully

take the hardware impairments as well as the environmental effects, such as water precipitations, flying debris, air particles, snowflakes, freezing rain, sleet, dry/damp sand particles and dirt into account, as shown in Fig. 1.

In practice, such blocking objects as well as the hardware impairments induce unwanted attenuation and phase shift on the reflected signals by the RIS introducing static or time-varying distortions in the received signal, which directly affect the channel estimation accuracy and, consequently, the system performance. However, the effects of hardware impairments and environmental imperfections have been rarely studied in the literature. For instance, [32]–[35], consider RISs operating under finite resolution of the phase shifts or phase estimation errors from imperfect channel estimation. Then, [36] and [37] consider different environmental effects on the RIS and propose methods to jointly estimate the channel and array blockage parameters in mmWave RIS-assisted systems.

As we explain in the following, typical channel estimation methods may not be able to deal with different imperfections and may fail to properly estimate the channel. Therefore, it is necessary to continuously monitor the channel and compensate for imperfections in order to maintain robust system operation.

In this paper, we propose tensor-based algorithms for the joint estimation of the involved channels and imperfections in RIS-assisted MIMO systems. We take both the long- and short-term imperfections into account. First, we show that the received signal under the long- and short-term imperfection models can be recast as tensors following trilinear and quadrilinear PARAFAC models, respectively. Exploiting the multi-linear structure of these models, we derive two sets of tensor-based algorithms. For the long-term imperfection (LTI) model, where the RIS imperfections, modeled as unknown phase shifts, are static within the channel coherence time, we formulate an iterative trilinear ALS-based algorithm, named TALS-LTI, for the joint estimation of the involved channels and the unknown RIS phase deviations. Next, we generalize the imperfections behavior to be non-static with respect to the channel coherence time, referred to as the short-term imperfection (STI) model. For such a more challenging scenario, we propose iterative and closed-form tensor decomposition-based algorithms named TALS-STI and HOSVD-STI, respectively, to solve the joint channel and RIS imperfections estimation. We also study the identifiability of the proposed estimators, discuss their computational complexity and investigate the effect of imperfections on the network performance. The key features of the proposed tensor-based algorithms are their ability to properly estimate the channel and their robustness to different kinds of real-world imperfections at the RIS.

The simulation results show that, compared to the state-of-the-art methods, the proposed algorithms properly estimate the involved channels when different kinds of imperfections are taken into account. As an example, in the high signal-to-noise ratio (SNR) regime, our proposed algorithms improve the channel estimation by approximately 100x compared to the method of [19], while present performance close to the lower-bound least squares (LS) estimator. Also, our proposed algorithms reduce considerably the overall computational complexity, compared to the related state-of-the-art method. Finally, the proposed TALS-LTI and TALS-STI algorithms are more flexible for the choices of training parameters compared

to the proposed HOSVD-STI algorithm. Thus, the TALS-LTI and TALS-STI algorithms are preferable when more flexible choices for training parameters are required, while the HOSVD-STI is preferred when low processing delay is desired.

The rest of this paper is organized as follows. In Section II, the signal model of the RIS-assisted MIMO communication system operating under imperfections is introduced. We distinguish between two different types of imperfections under the RIS operation, namely, LTI and STI. Then, the channel estimation problem is discussed for the LTI and STI scenarios. These signal models are reformulated as higher-order tensors that follow trilinear and quadrilinear PARAFAC models, from which two sets of iterative and closed-form tensor-based algorithms for the joint estimation of the involved channels and the RIS imperfections are developed in Section III. A detailed identifiability analysis and its link to the system design recommendations as well as the computational complexity of the proposed tensor-based algorithms are provided in Section IV. Simulation results are presented in Section V. Finally, conclusions are drawn in Section VI.

A. Notations and Properties

The notation conventions and the properties that will be used throughout this paper are defined in the following. Scalars are denoted by lower-case letters (a, b, \dots), column vectors by bold lower-case letters ($\mathbf{a}, \mathbf{b}, \dots$), matrices by bold upper-case letters ($\mathbf{A}, \mathbf{B}, \dots$) and tensors are represented by upper-case calligraphic letters ($\mathcal{A}, \mathcal{B}, \dots$). Then, \mathbf{A}^T and \mathbf{A}^\dagger stand for the transpose and Moore-Penrose pseudo-inverse of \mathbf{A} , respectively. The operator $\text{vec}(\cdot)$ vectorizes its matrix argument by stacking its columns on top of each other, while $\text{vecd}(\cdot)$ forms a vector out of the diagonal of its matrix argument. Also, $\|\cdot\|_F$ represents the Frobenius norm of a matrix or a tensor, which is defined as the square root of the sum of the squared of its elements. $\lceil x \rceil$ is equal to the smallest integer that is greater than or equal to x . Moreover, \mathbf{I}_M is the $M \times M$ identity matrix and $j = \sqrt{-1}$ is the imaginary unit. The operator $\mathbf{D}_i(\mathbf{A})$ forms a diagonal matrix from the i -th row of its matrix argument \mathbf{A} , while the operator $\text{diag}(\mathbf{a})$ forms a diagonal matrix out of its vector argument \mathbf{a} . We define the Kronecker, Hadamard (element-wise product) and the outer product operators by \otimes , \odot and \circ , respectively. The Khatri-Rao product (column-wise Kronecker product) between two matrices is defined as

$$\mathbf{A} \diamond \mathbf{B} = [\mathbf{a}_1 \otimes \mathbf{b}_1, \dots, \mathbf{a}_Q \otimes \mathbf{b}_Q] \in \mathbb{C}^{I \times J \times Q}, \quad (1)$$

or, equivalently,

$$\mathbf{A} \diamond \mathbf{B} = [\mathbf{D}_1(\mathbf{A})\mathbf{B}^T, \dots, \mathbf{D}_Q(\mathbf{A})\mathbf{B}^T]^T, \quad (2)$$

where $\mathbf{A} = [\mathbf{a}_1, \dots, \mathbf{a}_Q] \in \mathbb{C}^{I \times Q}$ and $\mathbf{B} = [\mathbf{b}_1, \dots, \mathbf{b}_Q] \in \mathbb{C}^{J \times Q}$.

We shall make use of the following properties of the Khatri-Rao and Kronecker products

$$\text{vec}(\mathbf{A} \text{diag}(\mathbf{c}) \mathbf{B}^T) = (\mathbf{B} \diamond \mathbf{A}) \mathbf{c}, \quad \forall \mathbf{A}, \mathbf{B}, \mathbf{c}, \quad (3)$$

$$\mathbf{a} \otimes \mathbf{b} \otimes \mathbf{c} = \text{vec}(\mathbf{c} \circ \mathbf{b} \circ \mathbf{a}), \quad \forall \mathbf{a}, \mathbf{b}, \mathbf{c}. \quad (4)$$

Furthermore, the definitions and operations involving tensors are in accordance with [38] and [39]. The n -mode

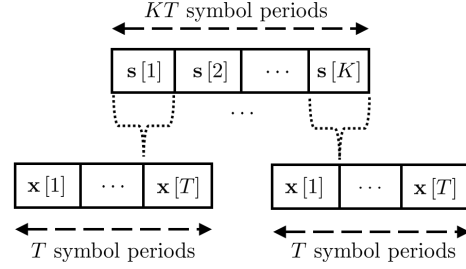


Fig. 2: An illustration of the considered channel estimation protocol. The training time is divided into K time-blocks of duration T symbol periods each. The RIS activation pattern $\mathbf{s}[k]$ is fixed during the k -th time-block and varies between different time-blocks while the pilot symbols $\mathbf{x}[1], \dots, \mathbf{x}[T]$ are reused from block-to-block.

unfolding matrix of \mathcal{A} along its n -th mode (or dimension) is represented by $[\mathcal{A}]_{(n)}$. The n -mode product between \mathcal{A} and \mathbf{B} , returns a tensor $\mathcal{C} = \mathcal{A} \times_n \mathbf{B}$ such that $[\mathcal{C}]_{(n)} = \mathbf{B} [\mathcal{A}]_{(n)}$.

II. SIGNAL MODEL AND PROBLEM DESCRIPTION

In this section, we first introduce the signal model and describe in detail the two considered LTI and STI models.

A. RIS Operating under LTI

We consider a single-user narrowband RIS-assisted MIMO communication system, in which the transmitter (Tx) and the receiver (Rx) are equipped with arrays composed of M and L antennas, respectively. Without loss of generality, although this work assumes a downlink communication, our signal models also apply to the uplink case by inverting the roles of the transmitter and the receiver. To improve the communication performance, an RIS with N individually adjustable passive reflecting elements is deployed in a proper place that creates an alternative Tx-RIS-Rx link. The direct Tx-Rx link is assumed to be too weak or unavailable due to unfavorable propagation conditions. The considered system setup is illustrated in Fig. 1. We also assume a block-fading channel where the Tx-RIS and RIS-Rx channels remain constant for at least $k = 1, \dots, K$, time-blocks, each with duration of T symbols, representing a total duration of KT symbol periods dedicated for channel estimation within the channel coherence time.

Let us define the RIS activation pattern $\mathbf{s}[k] \in \mathbb{C}^{N \times 1}$ configured at the k -th time-block as

$$\mathbf{s}[k] = [\beta_{1,k} e^{j\phi_{1,k}}, \dots, \beta_{N,k} e^{j\phi_{N,k}}]^T \in \mathbb{C}^{N \times 1}, \quad (5)$$

where $0 \leq \phi_{n,k} \leq 2\pi$ and $0 \leq \beta_{n,k} \leq 1$ denote the phase shift and the amplitude reflection coefficient of the n -th RIS element tuned at the k -th time-block $\forall n = 1, \dots, N$, and $\forall k = 1, \dots, K$, respectively. As a protocol for channel estimation we assume the following (see Fig. 2):

- 1) At each time-block $k = 1, \dots, K$, of duration T , the elements of $\mathbf{s}[k]$ are dynamically tuned in a passive way via the smart controller;
- 2) The activation pattern $\mathbf{s}[k]$ remains constant within the k -th time-block but may vary between different time-blocks, yielding a total of $\mathbf{s}[1], \dots, \mathbf{s}[K]$ different adjustable patterns to the RIS during the channel estimation stage;
- 3) The pilot symbol $\mathbf{x}[t, k] \in \mathbb{C}^{M \times 1}$ transmitted at the t -th symbol period within the k -th time-block is reused for each $k = 1, \dots, K$, i.e., $\mathbf{x}[t, k] = \mathbf{x}[t] \quad \forall k = 1, \dots, K$.

The baseband received pilot signal $\mathbf{y}[t, k] \in \mathbb{C}^{L \times 1}$ associated with the t -th symbol period at the k -th time-block can be expressed as

$$\mathbf{y}[t, k] = \mathbf{G} \text{diag}(\mathbf{s}[k]) \mathbf{H}^T \mathbf{x}[t] + \mathbf{v}[t, k]. \quad (6)$$

Collecting the received signals during the T symbol periods at the k -th time-block, the model in (6) can be rewritten as

$$\mathbf{Y}[k] = \mathbf{G} \text{diag}(\mathbf{s}[k]) \mathbf{H}^T \mathbf{X} + \mathbf{V}[k] \in \mathbb{C}^{L \times T}, \quad (7)$$

where $\mathbf{Y}[k] = [\mathbf{y}[1, k], \dots, \mathbf{y}[T, k]] \in \mathbb{C}^{L \times T}$. The matrices $\mathbf{H} \in \mathbb{C}^{M \times N}$ and $\mathbf{G} \in \mathbb{C}^{L \times N}$ denote the Tx-RIS and RIS-Rx channels, respectively, while $\mathbf{X} = [\mathbf{x}[1], \dots, \mathbf{x}[T]] \in \mathbb{C}^{M \times T}$ collects the pilot signals transmitted within the k -th time-block, and $\mathbf{V}[k] = [\mathbf{v}[1, k], \dots, \mathbf{v}[T, k]] \in \mathbb{C}^{L \times T}$ is the additive white Gaussian noise (AWGN) matrix with zero mean and unit variance elements. In order to simplify our formulation and analysis, without loss of generality, we assume the transmission of the pilot signal $\mathbf{X} = \mathbf{I}_M$.

In this work, a special attention is given to the structure of the RIS activation pattern. In practice, some imperfections at the RIS elements are common to occur. Initially, we assume the case in which such imperfections induce long-term static phase shift perturbations at the RIS response. Such imperfections may come from, e.g., phase noise due to the finite resolution of the phase shifts or by phase estimation errors from imperfect channel estimation. In the presence of these imperfections, the structure of the RIS activation pattern in (5) is modified in an undesired manner leading to the following resulting RIS reflection pattern that incorporates the imperfection contributions:

$$\bar{\mathbf{s}}[k] = \left[\beta_{1,k} e^{j(\phi_{1,k} + \theta_1)}, \dots, \beta_{N,k} e^{j(\phi_{N,k} + \theta_N)} \right]^T. \quad (8)$$

Here, $0 \leq \theta_n \leq 2\pi \forall n = 1, \dots, N$ denotes the phase shift perturbation that affects the n -th RIS element. Also, (8) can be alternatively represented in a more attractive form for our formulation as

$$\bar{\mathbf{s}}[k] = \mathbf{e} \odot \mathbf{s}[k] \in \mathbb{C}^{N \times 1}, \quad (9)$$

where the entries of the random vector $\mathbf{e} \in \mathbb{C}^{N \times 1}$ that collects all unknown existing phase perturbations are defined as

$$e_n = \begin{cases} 1, & \text{non-impaired case} \\ e^{j\theta_n}, & \text{otherwise,} \end{cases} \quad (10)$$

for $n = 1, \dots, N$. Making use of definitions in (9) and (10), the impaired version of the received signal at the Rx node in (7) can be expressed as

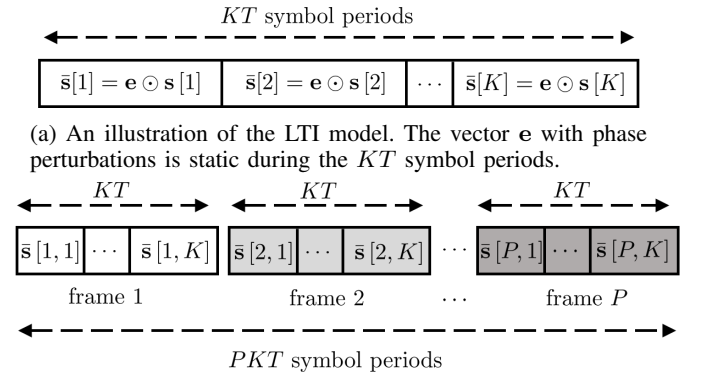
$$\mathbf{Y}[k] = \mathbf{G} \text{diag} \left(\underbrace{\mathbf{e} \odot \mathbf{s}[k]}_{\bar{\mathbf{s}}[k]} \right) \mathbf{H}^T + \mathbf{V}[k] \in \mathbb{C}^{L \times M}, \quad (11)$$

$\forall k = 1, \dots, K$. Equivalently, in matrix form we have

$$\mathbf{Y}[k] = \mathbf{G} \text{diag}(\mathbf{e}) \mathbf{D}_k(\mathbf{S}) \mathbf{H}^T + \mathbf{V}[k], \quad (12)$$

where $\mathbf{S} = [\mathbf{s}[1], \dots, \mathbf{s}[K]]^T \in \mathbb{C}^{K \times N}$ collects in its rows the RIS activation patterns used across K time-blocks specifically configured for the channel estimation.

Particularly, the impaired received signal in (12) considers an RIS operating under LTI that induces phase shift perturbations in the reflected signals. In other words, in this model we assume that the vector $\mathbf{e} \in \mathbb{C}^{N \times 1}$ is formed only by phase



(a) An illustration of the LTI model. The vector \mathbf{e} with phase perturbations is static during the KT symbol periods.

(b) An illustration of the generalized STI model with time-varying RIS fluctuations during the channel coherence time.

Fig. 3: Illustration of the LTI and STI models considered in the paper.

components that remain static within the KT symbol periods. Figure 3a illustrates the considered LTI model. This occurs, for instance, when the behavior of the imperfections at the RIS elements are static compared to the channel coherence time.

B. RIS Operating under STI

Here, we assume that the channel estimation occurs after the receiver collects $p = 1, \dots, P$ frames composed of KT symbol periods each. The division of the reception time into P frames is motivated by possible short-term variations caused by the RIS imperfections, i.e., the imperfections changing more frequently. In this approach, the behavior of the imperfections induces both amplitude and phase perturbations in the RIS elements and have a non-static nature with respect to channel coherence time but they present stationary characteristics within each frame. Figure 3b illustrates the considered STI model. In contrast to the received signal model formulated in (12), this assumption implies that such imperfection model takes into account rapid amplitude and phase fluctuations at the RIS elements during the channel coherence time. Note that the STI induces a block-fading effect in the signals reflected by the RIS during the PKT symbol periods for channel estimation. Therefore, by considering an RIS operating under this STI model the resulting reflection pattern related to the k -th time-block at the p -th frame can be written as

$$\bar{\mathbf{s}}[p, k] = [e_{n,p} \beta_{1,k} e^{j\phi_{1,k}}, \dots, e_{N,p} \beta_{N,k} e^{j\phi_{N,k}}]^T, \quad (13)$$

or, equivalently,

$$\bar{\mathbf{s}}[p, k] = \mathbf{e}[p] \odot \mathbf{s}[k] \in \mathbb{C}^{N \times 1}, \quad (14)$$

where $\mathbf{e}[p] = [e_{1,p}, \dots, e_{N,p}]^T \in \mathbb{C}^{N \times 1} \forall p = 1, \dots, P$, depends on the p -th received frame and models the unknown non-static amplitude and phase fluctuations along the training time. The entries of the random vector $\mathbf{e}[p]$ associated with the p -th frame are defined as

$$e_{n,p} = \begin{cases} 1, & \text{non-impaired case} \\ \alpha_{n,p} \cdot e^{j\theta_{n,p}}, & \text{otherwise,} \end{cases} \quad (15)$$

where $0 \leq \alpha_{n,p} \leq 1$ and $0 \leq \theta_{n,p} \leq 2\pi \forall n = 1, \dots, N$, and $\forall p = 1, \dots, P$, denote the unwanted amplitude attenuation and phase shift perturbations that affect the n -th RIS element at the p -th frame, respectively. It is important to note that the model

in (15) captures different kinds of real-world imperfections at the RIS. For example, we can note the follow situations:

- 1) $\alpha_{n,p} \neq 0$ and $\theta_{n,p} \neq 0$ represent the amplitude absorption and phase shift caused by an object suspended on the n -th RIS element [36], or caused by hardware impairments in the electronic circuits that make up the RIS [40].
- 2) $\alpha_{n,p} = 1$ and $\theta_{n,p} \neq 0$ represent the phase noise perturbations from low-resolution phase shifts or phase errors from imperfect channel estimation [32]- [35].
- 3) $\alpha_{n,p} = 0$ represents the maximum absorption i.e., the n -th RIS element is completely blocked [36].
- 4) $\alpha_{n,p} = 1$ and $\theta_{n,p} = 0$ represents the non-impaired RIS in which no imperfection affects its n -th element. Note that in this ideal case $\bar{s}[p, k] = \mathbf{s}[p, k]$ holds since $e_{n,p} = 1 \forall n = 1, \dots, N$, and $\forall p = 1, \dots, P$.

We also observe that the LTI model presented in Section II-A is a particular case of the generalized STI model when $\alpha_{n,p} = 1$ for $P = 1$ and $n = 1, \dots, N$. However, we study these two cases separately for a clearer description of the static and non-static imperfection scenarios.

By considering an RIS operating under the STI model, we can rewrite the received signal in (11) as

$$\mathbf{Y}[p, k] = \mathbf{G} \text{diag} \left(\underbrace{\mathbf{e}[p] \odot \mathbf{s}[k]}_{\bar{\mathbf{s}}[p, k]} \right) \mathbf{H}^T + \mathbf{V}[p, k], \quad (16)$$

$\forall p = 1, \dots, P$, and $\forall k = 1, \dots, K$. In a more convenient form for our formulation, the received signal (16) can be written in its complete matrix and decoupled format as

$$\mathbf{Y}[p, k] = \mathbf{G} \mathbf{D}_p(\mathbf{E}) \mathbf{D}_k(\mathbf{S}) \mathbf{H}^T + \mathbf{V}[p, k], \quad (17)$$

where each row of the matrix $\mathbf{E} = [\mathbf{e}[1], \dots, \mathbf{e}[P]]^T \in \mathbb{C}^{P \times N}$ collects the amplitude and phase parameters for the RIS elements impaired at the p -th frame. Throughout this work, for the two approaches formulated in Sections II-A and II-B, we assume that a number of $N_B = NR_B$ random elements at the RIS are subject to imperfections, where $R_B \in [0, 1]$ denotes its occurrence probability.

C. Problem Description

In (9) and (14), the RIS reflection pattern corrupted with errors $\bar{s}[k]$ and $\bar{s}[p, k]$ induce unwanted amplitude and/or phase shift responses in the reflected signal by the RIS creating a mismatch between the ideal reflection pattern and the one that is actually applied by the RIS. To deal with these imperfections, in this work we propose to jointly estimate the involved channels \mathbf{G} and \mathbf{H} , as well as the unknown imperfections that affect the N_B impaired elements at the RIS. Decoupled estimations of the channels are required, for instance, to optimize the phase shifts at the RIS, the transmit precoder at the transmitter and the receive combiner at the receiver in order to maximize the rate and energy efficiencies in the data transmission phase [16], [41]. However, the issues of how to utilize the estimated channels to jointly optimize the RIS phase shifts, the transmitter and receiver active beamformers, as well as the control overhead problem of optimal phase shifts [42], [43] are out of the scope of this work and will be addressed in a future work.

In the following, we show that the received signal models in (12) and (17) can be represented as third- and fourth-order tensor models, respectively. Then, we show how such higher-order representations serve as reference models for the development of efficient PARAFAC-based algorithms to solve the channel estimation problem for more realistic scenarios where the RIS operates under LTI and STI.

III. PROPOSED CHANNEL ESTIMATION ALGORITHMS

In this section, we propose three different channel estimation algorithms for the cases with LTI and STI.

A. TALS Algorithm for RIS Operating under LTI (TALS-LTI)

We initially consider the scenario with N_B unknown passive elements of the RIS being affected by LTI as presented in Section II-A. The values of the phase perturbations as well as their positions are assumed to be unknown at the receiver.

For simplicity of presentation and without loss of generality, we neglect the noise term in our formulations. The noiseless part of the received signal in (12) can be naturally identified as the k -th frontal slice of a third-order tensor $\mathcal{Y} \in \mathbb{C}^{L \times M \times K}$ that admits the following PARAFAC decomposition [38]

$$\mathcal{Y} = \mathcal{I}_{3,N} \times_1 \mathbf{G} \times_2 \mathbf{H} \times_3 \bar{\mathbf{S}}. \quad (18)$$

Here, $\mathcal{I}_{3,N}$ represents a third-order identity tensor of size $N \times N \times N$. According to (18), the factor matrices related to 1-mode, 2-mode and 3-mode of \mathcal{Y} are respectively $\mathbf{G} \in \mathbb{C}^{L \times N}$, $\mathbf{H} \in \mathbb{C}^{M \times N}$ and $\bar{\mathbf{S}} = [\bar{\mathbf{s}}[1], \dots, \bar{\mathbf{s}}[K]]^T \in \mathbb{C}^{K \times N}$ where according to (9), $\bar{\mathbf{s}}[k] = \mathbf{e} \odot \mathbf{s}[k]$ or, equivalently, in matrix notation $\mathbf{D}_k(\bar{\mathbf{S}}) = \text{diag}(\mathbf{e}) \mathbf{D}_k(\mathbf{S})$, $\forall k = 1, \dots, K$.

Resorting to the multilinear structure of the PARAFAC decomposition in (18), higher degrees of freedom for signal processing can be achieved by exploiting the dimensions of interest of the received signal tensor. In this sense, \mathcal{Y} can also be expressed with respect to its 1-mode and 2-mode unfoldings, which can be expressed as

$$[\mathcal{Y}]_{(1)} = \mathbf{G} \text{diag}(\mathbf{e}) (\mathbf{S} \diamond \mathbf{H})^T \in \mathbb{C}^{L \times MK}, \quad (19)$$

$$[\mathcal{Y}]_{(2)} = \mathbf{H} \text{diag}(\mathbf{e}) (\mathbf{S} \diamond \mathbf{G})^T \in \mathbb{C}^{M \times LK}, \quad (20)$$

where $[\mathcal{Y}]_{(1)} \in \mathbb{C}^{L \times MK}$ and $[\mathcal{Y}]_{(2)} \in \mathbb{C}^{M \times LK}$ are obtained from (12) by stacking the frontal slices into wide matrices, as defined by

$$[\mathcal{Y}]_{(1)} = [\mathbf{Y}[1], \dots, \mathbf{Y}[K]], \quad (21)$$

$$[\mathcal{Y}]_{(2)} = [\mathbf{Y}^T[1], \dots, \mathbf{Y}^T[K]]. \quad (22)$$

Additionally, (19) can also be represented in a convenient vectorized form. By applying the property (3) to (19) we obtain

$$\text{vec}([\mathcal{Y}]_{(1)}) = (\mathbf{S} \diamond \mathbf{H} \diamond \mathbf{G}) \mathbf{e} \in \mathbb{C}^{LMK \times 1}. \quad (23)$$

In the following, we describe an iterative way to estimate the channel matrices \mathbf{H} and \mathbf{G} from the received signal tensor \mathcal{Y} that models the RIS-assisted MIMO system with RIS operating under LTI. The estimation problem can be solved by computing a rank- N approximation to the PARAFAC decomposition of \mathcal{Y} , i.e.,

$$\min_{\mathbf{G}, \mathbf{H}, \mathbf{e}} \sum_{k=1}^K \|\mathbf{Y}[k] - \mathbf{G} \text{diag}(\mathbf{e}) \mathbf{D}_k(\mathbf{S}) \mathbf{H}^T\|_{\text{F}}^2. \quad (24)$$

Algorithm 1: TALS-LTI Algorithm

1. Set $i = 0$;
Keep \mathbf{S} fixed; Initialize randomly the matrix $\hat{\mathbf{H}}_{(i=0)}$
and the imperfections vector $\hat{\mathbf{e}}_{(i=0)}$;
2. $i \leftarrow i + 1$;
3. According to (28), obtain an LS estimate of $\hat{\mathbf{G}}_{(i)}$:

$$\hat{\mathbf{G}}_{(i)} = [\mathcal{Y}]_{(1)} \left[\text{diag}(\hat{\mathbf{e}}_{(i-1)}) (\mathbf{S} \diamond \hat{\mathbf{H}}_{(i-1)})^T \right]^\dagger;$$

4. According to (29), obtain an LS estimate of $\hat{\mathbf{H}}_{(i)}$:

$$\hat{\mathbf{H}}_{(i)} = [\mathcal{Y}]_{(2)} \left[\text{diag}(\hat{\mathbf{e}}_{(i-1)}) (\mathbf{S} \diamond \hat{\mathbf{G}}_{(i)})^T \right]^\dagger;$$

5. According to (30), obtain an LS estimate of $\hat{\mathbf{e}}_{(i)}$:

$$\hat{\mathbf{e}}_{(i)} = (\mathbf{S} \diamond \hat{\mathbf{H}}_{(i)} \diamond \hat{\mathbf{G}}_{(i)})^\dagger \text{vec}([\mathcal{Y}]_{(1)});$$

6. Calculate the residual error $\epsilon_{(i)} = \|\mathcal{Y}_{(1)} - [\hat{\mathcal{Y}}]_{(1)(i)}\|_F^2$
where

$$[\hat{\mathcal{Y}}]_{(1)(i)} = \hat{\mathbf{G}}_{(i)} \text{diag}(\hat{\mathbf{e}}_{(i)}) (\mathbf{S} \diamond \hat{\mathbf{H}}_{(i)})^T;$$

7. Repeat Steps 2-6 until $|\epsilon_{(i)} - \epsilon_{(i-1)}| \leq \delta$.
-

Problem (24) can be solved in an efficient form by an ALS algorithm [38], [44]. It is a well-known iterative method for estimating the factor matrices of a tensor model thanks to its implementation simplicity and monotonic convergence property in which the update of every given matrix at each iteration may either improve or maintain but cannot worsen the current fit, leading usually to global minimum solution [45], [46]. The decoupled estimates of \mathbf{G} , \mathbf{H} and \mathbf{e} can be obtained by converting the trilinear fitting problem in (24) into the following three simplest linear least squares (LS) sub-problems formulated from (19), (20) and (23), respectively

$$\hat{\mathbf{G}} = \underset{\mathbf{G}|\mathbf{e},\mathbf{H}}{\text{argmin}} \left\| [\mathcal{Y}]_{(1)} - \mathbf{G} \text{diag}(\mathbf{e}) (\mathbf{S} \diamond \mathbf{H})^T \right\|_F^2, \quad (25)$$

$$\hat{\mathbf{H}} = \underset{\mathbf{H}|\mathbf{e},\mathbf{G}}{\text{argmin}} \left\| [\mathcal{Y}]_{(2)} - \mathbf{H} \text{diag}(\mathbf{e}) (\mathbf{S} \diamond \mathbf{G})^T \right\|_F^2, \quad (26)$$

$$\hat{\mathbf{e}} = \underset{\mathbf{e}|\mathbf{H},\mathbf{G}}{\text{argmin}} \left\| \text{vec}([\mathcal{Y}]_{(1)}) - (\mathbf{S} \diamond \mathbf{H} \diamond \mathbf{G}) \mathbf{e} \right\|_F^2. \quad (27)$$

According to (25), the conditional LS update for $\hat{\mathbf{G}}$ is given by

$$\hat{\mathbf{G}} = [\mathcal{Y}]_{(1)} \left[\text{diag}(\mathbf{e}) (\mathbf{S} \diamond \mathbf{H})^T \right]^\dagger. \quad (28)$$

Similarly, according to (26) and (27), the conditional LS updates for $\hat{\mathbf{H}}$ and $\hat{\mathbf{e}}$ are respectively given by

$$\hat{\mathbf{H}} = [\mathcal{Y}]_{(2)} \left[\text{diag}(\mathbf{e}) (\mathbf{S} \diamond \mathbf{G})^T \right]^\dagger, \quad (29)$$

$$\hat{\mathbf{e}} = (\mathbf{S} \diamond \mathbf{H} \diamond \mathbf{G})^\dagger \text{vec}([\mathcal{Y}]_{(1)}). \quad (30)$$

The proposed TALS-STI algorithm consists of three iterative and alternating update steps formulated from the LS solutions in (28), (29) and (30). At each step, the fitting error is minimized with respect to one given factor matrix by fixing the other matrices to their values obtained at previous updating

steps. This procedure is repeated until the convergence of the algorithm at the i -th iteration determined by the designer.

Define

$$[\hat{\mathcal{Y}}]_{(1)(i)} = \hat{\mathbf{G}}_{(i)} \text{diag}(\hat{\mathbf{e}}_{(i)}) (\mathbf{S} \diamond \hat{\mathbf{H}}_{(i)})^T \in \mathbb{C}^{L \times MK}, \quad (31)$$

as the reconstructed version of $[\mathcal{Y}]_{(1)}$ obtained from the estimates of $\hat{\mathbf{G}}_{(i)}$, $\hat{\mathbf{H}}_{(i)}$, and $\hat{\mathbf{e}}_{(i)}$, and the residual error as

$$\epsilon_{(i)} = \left\| [\mathcal{Y}]_{(1)} - [\hat{\mathcal{Y}}]_{(1)(i)} \right\|_F^2, \quad (32)$$

computed at the end of the i -th iteration. The convergence of the algorithm is declared when $|\epsilon_{(i)} - \epsilon_{(i-1)}| \leq \delta$, with δ being a constant considered by the designer, meaning that the reconstruction error does not significantly change between two successive iterations. In this work, we set $\delta = 10^{-6}$ as a convergence threshold. The implementation steps of the proposed iterative TALS-LTI algorithm are summarized in the pseudocode shown in Algorithm 1. For the complexity analysis of Algorithm 1, see Section IV.

B. TALS Algorithm for RIS Operating under STI (TALS-STI)

In order to derive proposed channel estimators for a scenario with STI, let us first establish a link between the received signal in (17) and the PARAFAC decomposition. According to [38], the noiseless signal part of (17) expresses the (p, k) -th frontal slice of a fourth-order tensor $\mathcal{Y} \in \mathbb{C}^{L \times M \times K \times P}$ that follows the PARAFAC decomposition

$$\mathcal{Y} = \mathcal{I}_{4,N} \times_1 \mathbf{G} \times_2 \mathbf{H} \times_3 \mathbf{S} \times_4 \mathbf{E}. \quad (33)$$

Here, $\mathcal{I}_{4,N}$ denotes the fourth-order identity tensor of size $N \times N \times N \times N$, while \mathbf{G} , \mathbf{H} , \mathbf{S} and \mathbf{E} are the 1,2,3,4-mode factor matrices of the decomposition, respectively.

By stacking column-wise the noiseless received signal in (17) for the K time-blocks at frame p as the matrix $\mathbf{Y}_p = [\mathbf{Y}[p, 1], \dots, \mathbf{Y}[p, K]] \in \mathbb{C}^{L \times MK}$, we have

$$\mathbf{Y}_p = \mathbf{G} \mathbf{D}_p(\mathbf{E}) [\mathbf{D}_1(\mathbf{S}) \mathbf{H}^T, \dots, \mathbf{D}_K(\mathbf{S}) \mathbf{H}^T], \quad (34)$$

$\forall p = 1, \dots, P$. Applying the property (2) to the right-hand side of (34), a more compact form is obtained as

$$\mathbf{Y}_p = \mathbf{G} \mathbf{D}_p(\mathbf{E}) (\mathbf{S} \diamond \mathbf{H})^T \in \mathbb{C}^{L \times MK}. \quad (35)$$

From (35), we can define the new column-wise collection $[\mathcal{Y}]_{(1)} = [\mathbf{Y}_1, \dots, \mathbf{Y}_P] \in \mathbb{C}^{L \times MKP}$ as the 1-mode matrix unfolding of the received signal tensor $\mathcal{Y} \in \mathbb{C}^{L \times M \times K \times P}$ in (33), which is given by

$$[\mathcal{Y}]_{(1)} = \mathbf{G} \left[\mathbf{D}_1(\mathbf{E}) (\mathbf{S} \diamond \mathbf{H})^T, \dots, \mathbf{D}_P(\mathbf{E}) (\mathbf{S} \diamond \mathbf{H})^T \right]. \quad (36)$$

By applying property (2) to the right-hand side of (36), we finally obtain

$$[\mathcal{Y}]_{(1)} = \mathbf{G} (\mathbf{E} \diamond \mathbf{S} \diamond \mathbf{H})^T \in \mathbb{C}^{L \times MKP}. \quad (37)$$

Additionally, for our purpose, we also need to define the 2-mode, 3-mode and 4-mode matrix unfoldings of the fourth-order received signal tensor $\mathcal{Y} \in \mathbb{C}^{L \times M \times K \times P}$ since they will be exploited to formulate our second set of channel estimation algorithms in the sequel. The remaining unfoldings can be deduced using a similar procedure by permuting the factor matrices in (17). This leads to the following factorizations to the other unfoldings

$$[\mathcal{Y}]_{(2)} = \mathbf{H} (\mathbf{E} \diamond \mathbf{S} \diamond \mathbf{G})^T \in \mathbb{C}^{M \times LKP}, \quad (38)$$

$$[\mathcal{Y}]_{(3)} = \mathbf{S} (\mathbf{E} \diamond \mathbf{H} \diamond \mathbf{G})^T \in \mathbb{C}^{K \times LMP}, \quad (39)$$

$$[\mathcal{Y}]_{(4)} = \mathbf{E} (\mathbf{S} \diamond \mathbf{H} \diamond \mathbf{G})^T \in \mathbb{C}^{P \times LMK}. \quad (40)$$

In the following, we show that the channel matrices \mathbf{H} and \mathbf{G} can be also estimated when STI are assumed. From the received signal tensor described in (33), the estimates of \mathbf{G} and \mathbf{H} can be obtained by minimizing the following quadrilinear LS fitting problem

$$\min_{\mathbf{G}, \mathbf{H}, \mathbf{E}} \sum_{p=1}^P \sum_{k=1}^K \left\| \mathbf{Y} [p, k] - \mathbf{G} \mathbf{D}_p (\mathbf{E}) \mathbf{D}_k (\mathbf{S}) \mathbf{H}^T \right\|_F^2. \quad (41)$$

Similar to the TALS-LTI algorithm, we also propose to solve this optimization problem by means of the ALS algorithm. Since the matrix \mathbf{S} is known at the receiver, the quadrilinear fitting problem in (41) is simplified to a trilinear fitting problem that reduces to iteratively minimize the following linear LS sub-problems formulated from (37), (38) and (40), respectively

$$\hat{\mathbf{G}} = \underset{\mathbf{G} | \mathbf{E}, \mathbf{H}}{\operatorname{argmin}} \left\| [\mathcal{Y}]_{(1)} - \mathbf{G} (\mathbf{E} \diamond \mathbf{S} \diamond \mathbf{H})^T \right\|_F^2, \quad (42)$$

$$\hat{\mathbf{H}} = \underset{\mathbf{H} | \mathbf{E}, \mathbf{G}}{\operatorname{argmin}} \left\| [\mathcal{Y}]_{(2)} - \mathbf{H} (\mathbf{E} \diamond \mathbf{S} \diamond \mathbf{G})^T \right\|_F^2, \quad (43)$$

$$\hat{\mathbf{E}} = \underset{\mathbf{E} | \mathbf{H}, \mathbf{G}}{\operatorname{argmin}} \left\| [\mathcal{Y}]_{(4)} - \mathbf{E} (\mathbf{S} \diamond \mathbf{H} \diamond \mathbf{G})^T \right\|_F^2. \quad (44)$$

It follows from (42), (43) and (44) that the conditional LS updates of $\hat{\mathbf{G}}$, $\hat{\mathbf{H}}$ and $\hat{\mathbf{E}}$ are given by

$$\hat{\mathbf{G}} = [\mathcal{Y}]_{(1)} \left[(\mathbf{E} \diamond \mathbf{S} \diamond \mathbf{H})^T \right]^\dagger, \quad (45)$$

$$\hat{\mathbf{H}} = [\mathcal{Y}]_{(2)} \left[(\mathbf{E} \diamond \mathbf{S} \diamond \mathbf{G})^T \right]^\dagger, \quad (46)$$

$$\hat{\mathbf{E}} = [\mathcal{Y}]_{(4)} \left[(\mathbf{S} \diamond \mathbf{H} \diamond \mathbf{G})^T \right]^\dagger, \quad (47)$$

respectively. In the same way as in Algorithm 1, the updates of $\hat{\mathbf{G}}$, $\hat{\mathbf{H}}$ and $\hat{\mathbf{E}}$ are obtained by iteratively performing (45), (46) and (47) until the convergence. The proposed iterative TALS-STI algorithm is detailed in the pseudocode shown in Algorithm 2. For the complexity analysis of Algorithm 2, see Section IV.

Remark 1: In the application context of this work, the non-impaired RIS activation pattern matrix \mathbf{S} is assumed to be known at the receiver as indicated in the first step of Algorithms 1-2, respectively. This is a feasible assumption in accordance with the channel estimation protocol shown in Fig. 2. Among different design possibilities, we set \mathbf{S} as a semi-unitary matrix satisfying $\mathbf{S}^H \mathbf{S} = \mathbf{K} \mathbf{I}_N$. According to [29], a good choice is to consider \mathbf{S} as a deterministic truncated discrete Fourier transform (DFT) matrix. This choice guarantees a good performance of the proposed algorithms since the correlation properties of the additive noise are not affected during the estimation processing. More details on the optimal design of \mathbf{S} are found in [47]. Moreover, despite the iterative nature of the proposed TALS-LTI and TALS-STI algorithms, the convergence to the global minimum is always achieved within a few iterations (usually less than 80 iterations as verified in our simulation results) due to the knowledge of \mathbf{S} that remains fixed during the iterations.

Algorithm 2: TALS-STI Algorithm

1. Set $i = 0$;
Keep \mathbf{S} fixed;
Initialize randomly the matrices $\hat{\mathbf{H}}_{(i=0)}$ and $\hat{\mathbf{E}}_{(i=0)}$;
2. $i \leftarrow i + 1$;
3. According to (45), obtain an LS estimate of $\hat{\mathbf{G}}_{(i)}$:

$$\hat{\mathbf{G}}_{(i)} = [\mathcal{Y}]_{(1)} \left[\left(\hat{\mathbf{E}}_{(i-1)} \diamond \mathbf{S} \diamond \hat{\mathbf{H}}_{(i-1)} \right)^T \right]^\dagger;$$

4. According to (46), obtain an LS estimate of $\hat{\mathbf{H}}_{(i)}$:

$$\hat{\mathbf{H}}_{(i)} = [\mathcal{Y}]_{(2)} \left[\left(\hat{\mathbf{E}}_{(i-1)} \diamond \mathbf{S} \diamond \hat{\mathbf{G}}_{(i)} \right)^T \right]^\dagger;$$

5. According to (47), obtain an LS estimate of $\hat{\mathbf{E}}_{(i)}$:

$$\hat{\mathbf{E}}_{(i)} = [\mathcal{Y}]_{(4)} \left[\left(\mathbf{S} \diamond \hat{\mathbf{H}}_{(i)} \diamond \hat{\mathbf{G}}_{(i)} \right)^T \right]^\dagger;$$

6. Calculate the residual error $\epsilon_{(i)} = \left\| [\mathcal{Y}]_{(1)} - [\hat{\mathcal{Y}}]_{(1)(i)} \right\|_F^2$ where

$$[\hat{\mathcal{Y}}]_{(1)(i)} = \hat{\mathbf{G}}_{(i)} \left(\hat{\mathbf{E}}_{(i)} \diamond \mathbf{S} \diamond \hat{\mathbf{H}}_{(i)} \right)^T;$$

7. Repeat Steps 2-6 until $|\epsilon_{(i)} - \epsilon_{(i-1)}| \leq \delta$.
-

C. HOSVD Algorithm for RIS Operating under STI (HOSVD-STI)

We now derive a closed-form solution based on higher order singular value decomposition (HOSVD) for channel estimation under the STI model. According to (39), the transpose of the 3-mode unfolding of \mathcal{Y} is denoted by

$$[\mathcal{Y}]_{(3)}^T = (\mathbf{E} \diamond \mathbf{H} \diamond \mathbf{G}) \mathbf{S}^T. \quad (48)$$

The first processing step at the receiver is to apply a bilinear time-domain matched-filtering by multiplying both sides in (48) by the pseudo-inverse of \mathbf{S}^T , resulting in

$$\tilde{\mathbf{Y}} = \mathbf{E} \diamond \mathbf{H} \diamond \mathbf{G} \in \mathbb{C}^{LMP \times N}, \quad (49)$$

where $\tilde{\mathbf{Y}} = [\mathcal{Y}]_{(3)}^T (\mathbf{S}^T)^\dagger$. From (49), decoupled estimates of the channel matrices and RIS imperfections can be obtained by separating each factor matrix in the Khatri-Rao product. In this sense, the estimates can be obtained by minimizing the following cost function

$$\min_{\mathbf{G}, \mathbf{H}, \mathbf{E}} \left\| \tilde{\mathbf{Y}} - \mathbf{E} \diamond \mathbf{H} \diamond \mathbf{G} \right\|_F^2. \quad (50)$$

Here, we propose to solve this problem by means of multiple rank-one tensor approximations via the HOSVD [39]. To this end, let us define $\tilde{\mathbf{Y}} = [\tilde{\mathbf{y}}_1, \dots, \tilde{\mathbf{y}}_N] \in \mathbb{C}^{LMP \times N}$, and note that according to (1), the n -th column of $\tilde{\mathbf{Y}}$ can be written as

$$\tilde{\mathbf{y}}_n = \mathbf{e}_n \otimes \mathbf{h}_n \otimes \mathbf{g}_n \in \mathbb{C}^{LMP \times 1}, \quad (51)$$

where $\mathbf{e}_n \in \mathbb{C}^{P \times 1}$, $\mathbf{h}_n \in \mathbb{C}^{M \times 1}$ and $\mathbf{g}_n \in \mathbb{C}^{L \times 1}$ denote the n -th column of \mathbf{E} , \mathbf{H} and \mathbf{G} , respectively. Using the equivalence property in (4) that relates the Kronecker product to the outer product, we can rewrite (51) as

$$\tilde{\mathbf{y}}_n = \operatorname{vec} (\mathbf{g}_n \circ \mathbf{h}_n \circ \mathbf{e}_n) \in \mathbb{C}^{LMP \times 1}, \quad (52)$$

that represents the vectorized form of the following third-order rank-one tensor

Algorithm 3: HOSVD-STI Algorithm

for $n = 1, \dots, N$

1. Rearrange the n -th column of $\tilde{\mathbf{Y}}$ in Equation (49) as the rank-one tensor $\tilde{\mathcal{Y}}_n$ in Equation (53);

2. HOSVD procedure

2.1 Compute $\mathbf{U}_n^{(1)}$ as the L left singular vectors of $[\tilde{\mathcal{Y}}_n]_{(1)}$:

$$[\tilde{\mathcal{Y}}_n]_{(1)} = \mathbf{U}_n^{(1)} \cdot \boldsymbol{\Sigma}_n^{(1)} \cdot \mathbf{V}_n^{(1)H};$$

2.2 Compute $\mathbf{U}_n^{(2)}$ as the M left singular vectors of $[\tilde{\mathcal{Y}}_n]_{(2)}$:

$$[\tilde{\mathcal{Y}}_n]_{(2)} = \mathbf{U}_n^{(2)} \cdot \boldsymbol{\Sigma}_n^{(2)} \cdot \mathbf{V}_n^{(2)H};$$

2.3 Compute $\mathbf{U}_n^{(3)}$ as the P left singular vectors of $[\tilde{\mathcal{Y}}_n]_{(3)}$:

$$[\tilde{\mathcal{Y}}_n]_{(3)} = \mathbf{U}_n^{(3)} \cdot \boldsymbol{\Sigma}_n^{(3)} \cdot \mathbf{V}_n^{(3)H};$$

2.4 Compute the HOSVD core tensor \mathcal{G}_n as:

$$\mathcal{G}_n = \tilde{\mathcal{Y}}_n \times_1 \mathbf{U}_n^{(1)H} \times_2 \mathbf{U}_n^{(2)H} \times_3 \mathbf{U}_n^{(3)H};$$

end procedure

3. Obtain the estimates for $\hat{\mathbf{g}}_n$, $\hat{\mathbf{h}}_n$ and $\hat{\mathbf{e}}_n$ from Equations (56), (57) and (58), respectively;

end

4. Return the matrices $\hat{\mathbf{G}} = [\hat{\mathbf{g}}_1, \dots, \hat{\mathbf{g}}_N]$, $\hat{\mathbf{H}} = [\hat{\mathbf{h}}_1, \dots, \hat{\mathbf{h}}_N]$ and $\hat{\mathbf{E}} = [\hat{\mathbf{e}}_1, \dots, \hat{\mathbf{e}}_N]$.

$$\tilde{\mathcal{Y}}_n = \mathbf{g}_n \circ \mathbf{h}_n \circ \mathbf{e}_n \in \mathbb{C}^{L \times M \times P}. \quad (53)$$

Thus, the optimization problem in (50) is equivalent to finding the estimates of \mathbf{H} , \mathbf{G} and \mathbf{E} that minimize a set of N rank-one tensor approximations, i.e.,

$$\left(\hat{\mathbf{G}}, \hat{\mathbf{H}}, \hat{\mathbf{E}} \right) = \underset{\mathbf{G}, \mathbf{H}, \mathbf{E}}{\operatorname{argmin}} \sum_{n=1}^N \left\| \tilde{\mathcal{Y}}_n - \mathbf{g}_n \circ \mathbf{h}_n \circ \mathbf{e}_n \right\|_{\mathbb{F}}^2. \quad (54)$$

Let us introduce the HOSVD of $\tilde{\mathcal{Y}}_n$ as

$$\tilde{\mathcal{Y}}_n = \mathcal{G}_n \times_1 \mathbf{U}_n^{(1)} \times_2 \mathbf{U}_n^{(2)} \times_3 \mathbf{U}_n^{(3)} \in \mathbb{C}^{L \times M \times P}, \quad (55)$$

where $\mathbf{U}_n^{(1)} \in \mathbb{C}^{L \times L}$, $\mathbf{U}_n^{(2)} \in \mathbb{C}^{M \times M}$ and $\mathbf{U}_n^{(3)} \in \mathbb{C}^{P \times P}$ are unitary matrices, while $\mathcal{G}_n \in \mathbb{C}^{L \times M \times P}$ denotes the HOSVD core tensor. The estimates of the vectors \mathbf{g}_n , \mathbf{h}_n and \mathbf{e}_n that solve the LS problem in (54) can be obtained by truncating the HOSVD of $\tilde{\mathcal{Y}}_n$ to its dominant rank-one component, yielding

$$\hat{\mathbf{g}}_n = \sqrt[3]{(\mathcal{G}_n)_{1,1,1}} \cdot \mathbf{u}_{1,n}^{(1)}, \quad (56)$$

$$\hat{\mathbf{h}}_n = \sqrt[3]{(\mathcal{G}_n)_{1,1,1}} \cdot \mathbf{u}_{1,n}^{(2)}, \quad (57)$$

$$\hat{\mathbf{e}}_n = \sqrt[3]{(\mathcal{G}_n)_{1,1,1}} \cdot \mathbf{u}_{1,n}^{(3)}, \quad (58)$$

where $\mathbf{u}_{1,n}^{(1)} \in \mathbb{C}^{L \times 1}$, $\mathbf{u}_{1,n}^{(2)} \in \mathbb{C}^{M \times 1}$ and $\mathbf{u}_{1,n}^{(3)} \in \mathbb{C}^{P \times 1}$ are the first higher order singular vectors, i.e., the first column of $\mathbf{U}_n^{(1)}$, $\mathbf{U}_n^{(2)}$ and $\mathbf{U}_n^{(3)}$, respectively. Here, $(\mathcal{G}_n)_{1,1,1}$ is the first element of the core tensor \mathcal{G}_n . The estimates of $\hat{\mathbf{G}}$, $\hat{\mathbf{H}}$ and $\hat{\mathbf{E}}$ are obtained by repeating the procedure of (53)-(58) for the N columns of $\tilde{\mathbf{Y}}$ in (49). In other words, a total of N rank-one tensor approximations via HOSVD are necessary

to obtain the full estimates of the matrices $\hat{\mathbf{G}} = [\hat{\mathbf{g}}_1, \dots, \hat{\mathbf{g}}_N]$, $\hat{\mathbf{H}} = [\hat{\mathbf{h}}_1, \dots, \hat{\mathbf{h}}_N]$ and $\hat{\mathbf{E}} = [\hat{\mathbf{e}}_1, \dots, \hat{\mathbf{e}}_N]$ in a closed-form manner. The implementation steps of the proposed closed-form HOSVD-STI algorithm are summarized in Algorithm 3. For the complexity analysis of Algorithm 3, see Section IV.

IV. IDENTIFIABILITY AND COMPUTATIONAL COMPLEXITY

In this section, we examine the identifiability aspects and the computational complexity associated with the proposed tensor-based TALS-LTI, TALS-STI and HOSVD-STI algorithms.

1) *TALS-LTI algorithm:* According to (28) and (29), the uniqueness of the LS estimates of $\hat{\mathbf{G}}$ and $\hat{\mathbf{H}}$ requires that $\operatorname{diag}(\mathbf{e})(\mathbf{S} \diamond \mathbf{H})^T \in \mathbb{C}^{N \times KM}$ and $\operatorname{diag}(\mathbf{e})(\mathbf{S} \diamond \mathbf{G})^T \in \mathbb{C}^{N \times KL}$ are full row-rank to be right-invertible. Additionally, the uniqueness of the LS estimate of $\hat{\mathbf{e}}$ requires that $(\mathbf{S} \diamond \mathbf{H} \diamond \mathbf{G}) \in \mathbb{C}^{KLM \times N}$ be full column-rank to be left-invertible in (30). This means that the conditions $N \leq KM$, $N \leq KL$ and $N \leq KLM$ must be jointly satisfied. By combining these three necessary and sufficient conditions, we obtain the lower bound on the number of time-blocks K necessary for channel estimation so that Steps 3, 4 and 5 in Algorithm 1 yield unique solutions:

$$K \geq \left\lceil \frac{N}{\min(L, M)} \right\rceil. \quad (59)$$

2) *TALS-STI algorithm:* We can note from (45), (46) and (47) that unique estimates of $\hat{\mathbf{G}}$, $\hat{\mathbf{H}}$ and $\hat{\mathbf{E}}$ in the LS sense requires that $(\mathbf{E} \diamond \mathbf{S} \diamond \mathbf{H})^T \in \mathbb{C}^{N \times KMP}$, $(\mathbf{E} \diamond \mathbf{S} \diamond \mathbf{G})^T \in \mathbb{C}^{N \times KLP}$ and $(\mathbf{S} \diamond \mathbf{H} \diamond \mathbf{G})^T \in \mathbb{C}^{N \times KLM}$ are full row-rank to be right-invertible. This means that the conditions $N \leq KMP$, $N \leq KLP$ and $N \leq KLM$ must be satisfied. The combination of these inequalities leads to the following necessary and sufficient condition to be satisfied

$$K \geq \left\lceil \frac{N}{\min(MP, LP, LM)} \right\rceil. \quad (60)$$

The condition in (60) establishes the lower-bound on the required number of time-blocks K so that Steps 3, 4 and 5 in Algorithm 2 provide unique solutions when STI are assumed.

3) *HOSVD-STI algorithm:* In contrast to the iterative TALS-LTI and TALS-STI algorithms in which three LS conditions must be jointly satisfied, the proposed HOSVD-STI algorithm is a closed-form solution requiring only that the RIS activation pattern matrix $\mathbf{S} \in \mathbb{C}^{K \times N}$ has full column-rank in order to guarantee the uniqueness in the LS sense when the bilinear time-domain matched-filtering preprocessing is performed at the receiver side, as indicated in (49). This leads to the following necessary and sufficient condition to the use of the HOSVD-STI algorithm

$$K \geq N. \quad (61)$$

This condition is satisfied under the truncated DFT design discussed in *Remark 1*, where the RIS activation pattern matrix has orthonormal columns.

According to (59)-(61), independent of the imperfection model, the required number of time-blocks K scales with the number of RIS elements N at least linearly. However, the proposed TALS-LTI and TALS-STI algorithms present more flexible operation conditions for channel estimation compared to our HOSVD-STI algorithm. On the other hand,

the HOSVD-STI is a closed-form approach that presents lower computational complexity compared to the others one, as discussed in the following.

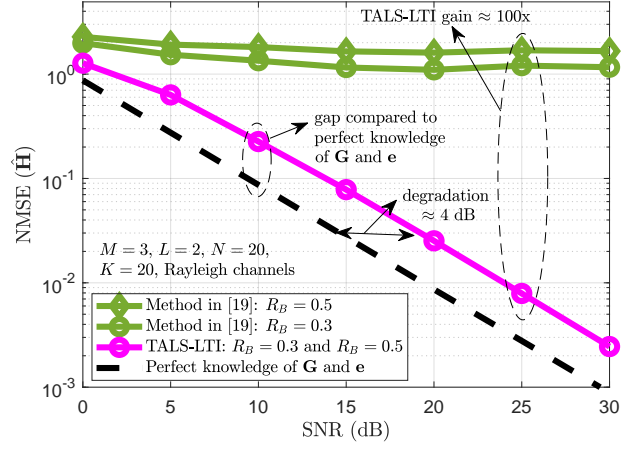
4) *Computational complexity*: As can be observed in Algorithms 1-2, the computational complexity of the proposed TALS-LTI and TALS-STI algorithms is dominated by the cost associated with the computation of the matrix pseudo-inverses in three LS update steps that calculate the estimates of the channels and imperfection matrices in an iterative and alternating way. Therefore, the computational complexity of the TALS-LTI and TALS-STI algorithms are $\mathcal{O}(N^2K[M+L+ML])$ and $\mathcal{O}(N^2K[PM+PL+ML])$ per iteration, respectively. Regarding the proposed HOSVD-STI in Algorithm 3, its computational complexity is dominated by the HOSVD of the third-order rank-one tensor in (53), which is equivalent to compute the truncated SVDs of its 1-mode, 2-mode and 3-mode unfolding matrices to rank-one. These truncated SVDs are repeated N times. Therefore, the HOSVD-STI algorithm has a complexity $\mathcal{O}(NMLP)$, which is clearly less than that of the TALS-LTI and TALS-STI algorithms. Specially, as opposed to Algorithms 1-2, where the computational complexity is proportional to N^2 , in Algorithm 3 the complexity scales with the RIS size N linearly. As a result, compared to Algorithms 1-2, the relative gain of Algorithm 3, in terms of complexity increases rapidly as the number of RIS elements increases.

Remark 2: By comparing the conditions in (60) and (61), we observe that the TALS-STI algorithm presents a less restrictive requirement on the minimum number K of time-blocks necessary for the channel estimation compared to HOSVD-STI algorithm that works well when $K \geq N$ is satisfied. On the other hand, in the HOSVD-STI algorithm a single HOSVD is computed independently for each column of the post-filtered signal in (49). This leads to a total of N independent rank-one tensor approximations via HOSVD that can be parallelized if more than one processor is available leading to a considerable reduction in the total processing time for channel estimation. Based on this, we can conclude that the TALS-STI algorithm may be preferred in situations where more flexible choices for the number of time-blocks, K , are required while the HOSVD-STI algorithm becomes more attractive when low processing delay is needed and the receiver is equipped with multiple processors. Hence, there is a tradeoff between computational complexity and operation conditions for the proposed tensor-based algorithms.

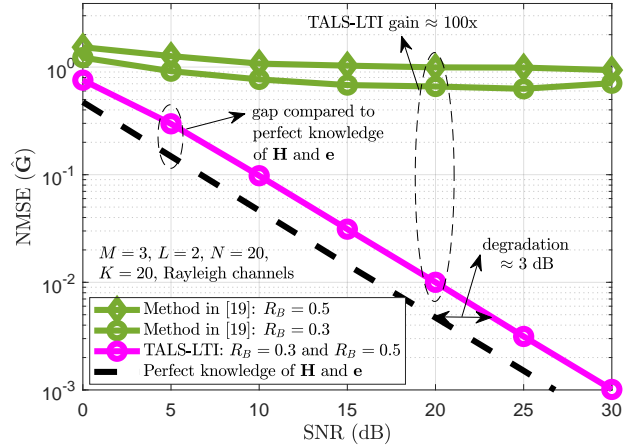
Remark 3: Since \mathbf{S} is known at the receiver, by satisfying the design recommendations given by (59), (60) and (61) the estimated factor matrices $\hat{\mathbf{G}}$, $\hat{\mathbf{H}}$ and $\hat{\mathbf{E}}$ do not suffer from column permutation ambiguity. The scaling ambiguity affecting the columns of the estimated matrices can be eliminated with a simple normalization procedure, as performed in [22] and [29].

V. SIMULATION RESULTS

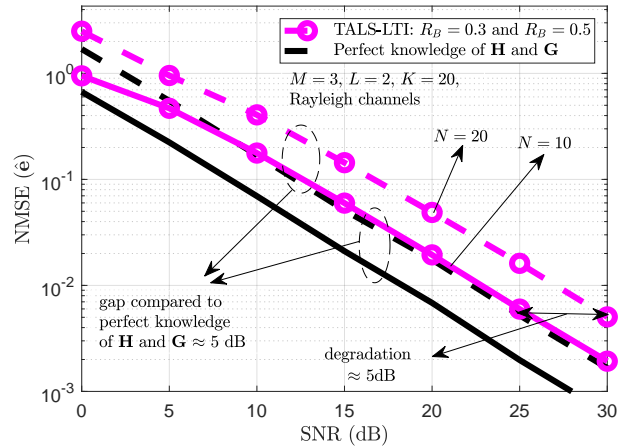
In this section, we present the simulation results for performance evaluation of our proposed tensor-based algorithms, in terms of computational complexity and estimation accuracy of the channels and imperfections, while comparing to benchmark approaches. The results presented here are averaged over $\Omega = 3 \cdot 10^3$ independent Monte Carlo runs. Each run corresponds to a different realization of the involved communication



(a) NMSE of $\hat{\mathbf{H}}$ versus SNR (dB).



(b) NMSE of $\hat{\mathbf{G}}$ versus SNR (dB).



(c) NMSE of $\hat{\mathbf{e}}$ versus SNR (dB).

Fig. 4: NMSE performance of the TALS-LTI algorithm versus the SNR (dB) for $M = 3$ transmit antennas, $L = 2$ receive antennas, $K = 20$ time-blocks and different RIS elements N and impairments occurrence probability R_B assuming i.i.d. Rayleigh fading channels.

channels, RIS patterns, impairment parameters and noise. We have designed the RIS pattern matrix \mathbf{S} as a DFT matrix. The amplitude and phase impairments parameters embedded in the

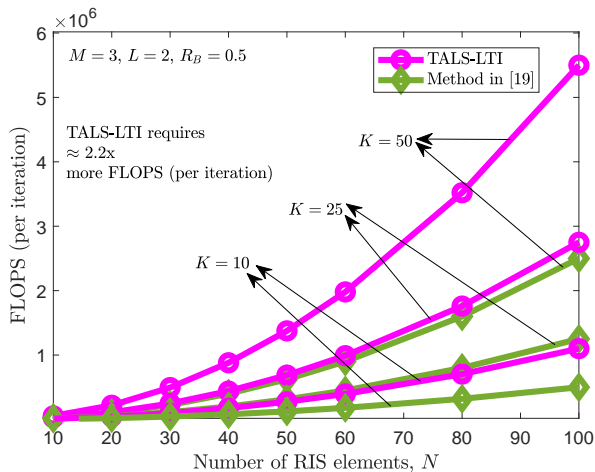


Fig. 5: Number of FLOPs required by the TALS-LTI algorithm versus the number of the RIS elements N for $M = 3$ transmit antennas, $L = 2$ receive antennas, impairments occurrence probability $R_B = 0.5$ and different time-blocks K .

vector \mathbf{e} and in the matrix \mathbf{E} follow a uniform distribution between $[0, 1]$ and between $[0, 2\pi]$, respectively. The location of the unknown N_B impaired elements are assumed to be random with occurrence probability R_B , totalizing $N_B = NR_B$ impaired elements at the RIS in each simulated setup. The metric used to evaluate the estimation accuracy is the normalized mean square error (NMSE) between the true and estimated matrices that provides a relative measure for the estimation error of the proposed algorithms. For the estimated channel $\hat{\mathbf{H}}$, we define

$$\text{NMSE}(\hat{\mathbf{H}}) = \frac{1}{\Omega} \sum_{\omega=1}^{\Omega} \frac{\|\mathbf{H}^{(\omega)} - \hat{\mathbf{H}}^{(\omega)}\|_F^2}{\|\mathbf{H}^{(\omega)}\|_F^2}, \quad (62)$$

where $\mathbf{H}^{(\omega)}$ and $\hat{\mathbf{H}}^{(\omega)}$ denote the true channel and its estimate both related to the ω -th run, respectively. Similar definitions as in (62) apply to the estimates of $\hat{\mathbf{G}}$, $\hat{\mathbf{E}}$ and $\hat{\mathbf{e}}$. Finally, note that, while we present the simulation results for a set of parameter settings, we have test the results for a broad range of parameter settings and observed the same qualitative conclusions as those presented.

A. TALS-LTI Performance

We first examine, in Figs. 4 and 5, the performance of the proposed TALS-LTI algorithm. These plots show the NMSE and computational complexity in terms of floating-point operations (FLOPs) assuming i.i.d. Rayleigh fading channels. As a benchmark, we compare our TALS-LTI algorithm with the method proposed in [19], which is also a PARAFAC-based algorithm but formulated to the ideal case in which no impairments affect the RIS elements. Additionally, as a lower-bound for comparison, we also plot the performance of the *clairvoyant* LS estimators of $\hat{\mathbf{H}}$, $\hat{\mathbf{G}}$ and $\hat{\mathbf{e}}$ in (28), (29) and (30) obtained when the true factor matrices in the right-hand side of these equations are perfectly known.

From Figs. 4a and 4b, we can observe that the method in [19] is not suitable to tackle the channel estimation problem when RIS impairments are present. In contrast, our proposed TALS-LTI algorithm provides accurate estimates in which the

NMSE of the estimated channels decreases linearly when the SNR increases, and is not sensitive to the number of impaired elements at the RIS. For instance, the TALS-LTI presents constant gaps when compared to the lower-bound LS estimator equal to 4 dB and 3 dB providing satisfactory performance in terms of the channel estimation for all simulated SNR range. Also, in contrast to method in [19], the TALS-LTI accurately estimates the RIS impairments that are treated as independent variables estimated beyond the involved channels, as illustrated in Fig. 4c.

In terms of computational complexity, we can see from Fig. 5 that the TALS-LTI presents greater complexity than competitor method requiring approximately 2.2x more FLOPs per iteration. This happens because the TALS-LTI has one more update step (per iteration) to estimate the RIS imperfections compared to the method in [19] that does not perform the estimation of imperfections. Also, the complexity of both approaches increases with the number of RIS elements N and time-blocks K .

B. TALS-STI and HOSVD-STI Performance

Here, we evaluate the performance of the proposed TALS-STI and HOSVD-STI algorithms assuming i.i.d. Rayleigh fading channels and a typical mmWave propagation environment. For the mmWave setup, we assume that the transmitter and the receiver are equipped with half-wavelength spaced uniform linear arrays while the RIS has half-wavelength spaced reflecting elements disposed in a uniform rectangular grid. In this case, the channel matrices are generated according to the widely used geometric channel model [7], in which the angles of arrival and departure are randomly generated according to a uniform distribution. The azimuth and elevation angles are drawn between $[-\pi/2, \pi/2]$ and $[0, \pi/2]$, respectively. The number of propagation paths is set to 1 in the Tx-RIS link and to 2 in the RIS-Rx link, respectively. The complex channel gains follow uniform distributions. The lower-bound LS estimators of $\hat{\mathbf{H}}$, $\hat{\mathbf{G}}$ and $\hat{\mathbf{E}}$ are obtained similarly to Section V-A, but now from (45), (46) and (47), respectively.

From Fig. 6, similar conclusions to the results in Fig. 4, in terms of channel estimation performance, can be made by comparing the proposed TALS-STI and HOSVD-STI algorithms with the method in [19]. However, more accurate estimates for the channels and impairments are obtained when the mmWave propagation scenario is considered. In this experiment, the TALS-STI and HOSVD-STI present, respectively, constant gaps of approximately 1 dB and 2 dB, compared to the lower-bound LS estimator for the considered range of SNR, confirming the effectiveness of the proposed tensor-based algorithms in terms of estimation accuracy. Similar results are obtained for the proposed TALS-LTI algorithm, but omitted here due to space limitation. Also, we see from Fig. 6c, that in the low/medium SNR regime, the TALS-STI algorithm outperforms the HOSVD-STI one in terms of imperfections estimation, indicating that the TALS-STI algorithm becomes preferable with considerable gain in low SNR when complexity issues are not taken into account. The tradeoff between computational complexity and estimation performance is analyzed in the sequel. The presented result indicates that the proposed algorithms are able to work with high accuracy under different propagation environments and

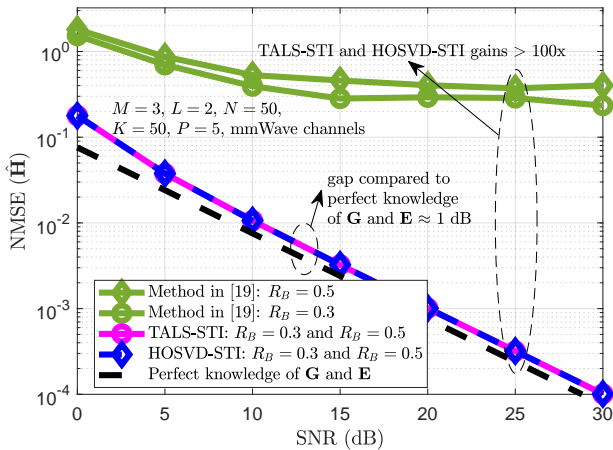
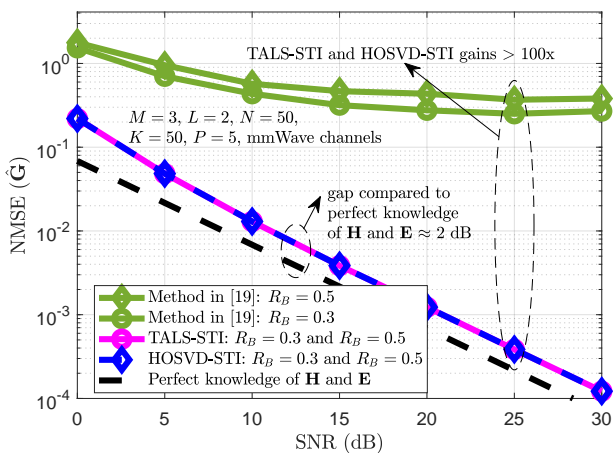
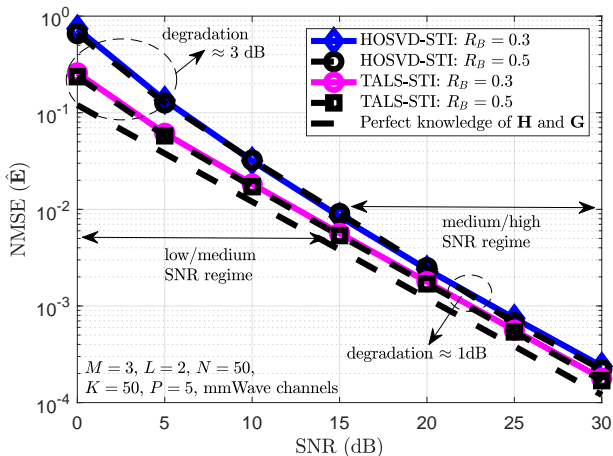
(a) NMSE of $\hat{\mathbf{H}}$ versus SNR (dB).(b) NMSE of $\hat{\mathbf{G}}$ versus SNR (dB).(c) NMSE of $\hat{\mathbf{E}}$ versus SNR (dB).

Fig. 6: NMSE performance of the TALS-STI and HOSVD-STI algorithms versus the SNR (dB) for $M = 3$ transmit antennas, $L = 2$ receive antennas, $N = 50$ RIS elements, $K = 50$ time-blocks, $P = 5$ frames and different impairments occurrence probability R_B assuming a typical mmWave propagation environment.

kinds of imperfections, i.e., our approaches are general techniques that provide accurate estimates for different channel

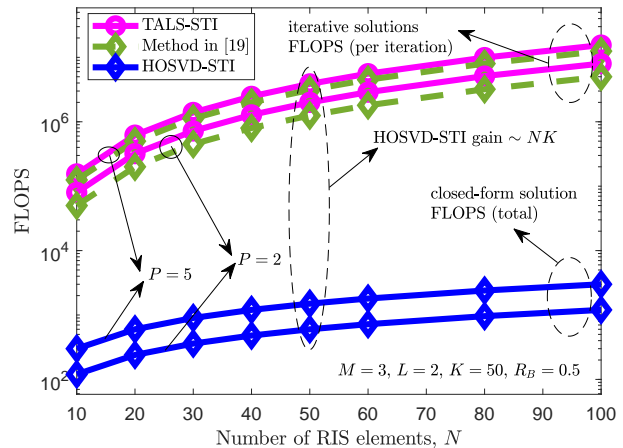


Fig. 7: Number of FLOPs required by the TALS-STI and HOSVD-STI algorithms versus the number of the RIS elements N for $M = 3$ transmit antennas, $L = 2$ receive antennas, $K = 50$ time-blocks, impairments occurrence probability $R_B = 0.5$ and different frames P .

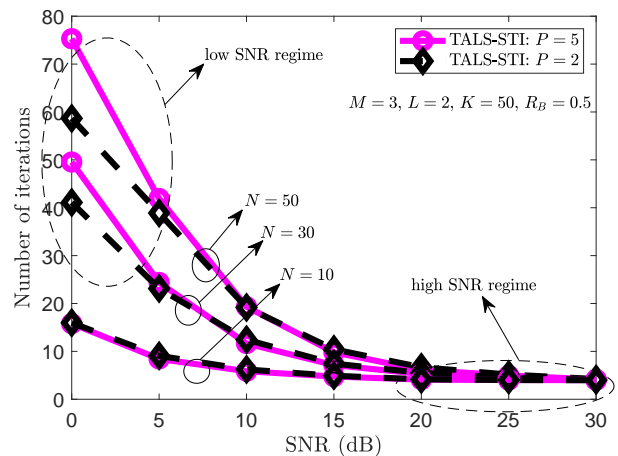


Fig. 8: Number of iterations required by the TALS-STI algorithm versus the SNR (dB) for $M = 3$ transmit antennas, $L = 2$ receive antennas, $K = 50$ time-blocks, impairments occurrence probability $R_B = 0.5$ and different RIS elements N and frames P .

models.

In Fig. 7, we evaluate the computational complexity (in terms of FLOPs) of the TALS-STI and HOSVD-STI algorithms. We can see that the HOSVD-STI is less complex than TALS-STI for different values of RIS elements N and frames P , since it is a closed-form solution for joint channel and imperfections estimation. The HOSVD-STI algorithm provides a remarkable gain of the order of NK FLOPs compared to the TALS-STI one. It can be seen that the complexity of both methods grows when the number of RIS elements N and frames P increases, which is an expected result since the number of entries in \mathbf{H} , \mathbf{G} and \mathbf{E} also increases with N and P . However, in contrast to the HOSVD-STI which is a closed-form solution, for a complete analysis on the overall complexity of the proposed techniques, Fig. 8 shows the number of iterations necessary for the convergence of the TALS-STI algorithm considering different values of N

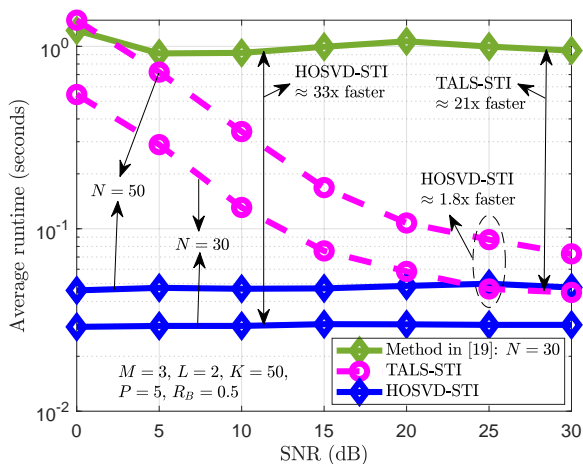
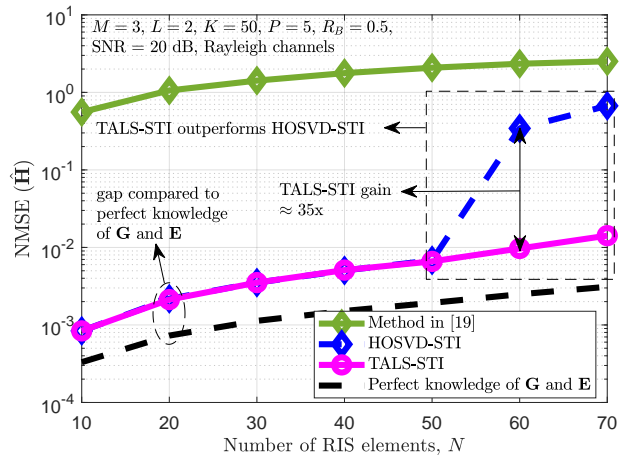


Fig. 9: Average runtime (in seconds) for the TALS-STI and HOSVD-STI algorithms versus the SNR (dB) for $M = 3$ transmit antennas, $L = 2$ receive antennas, $K = 50$ time-blocks, $P = 5$ frames, impairments occurrence probability $R_B = 0.5$ and different RIS elements N .

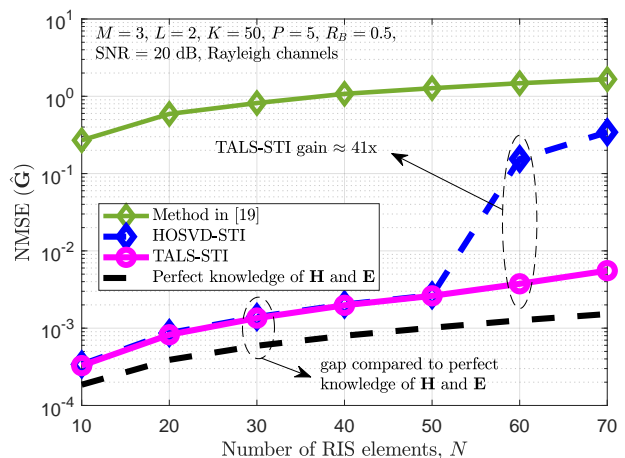
and P . It can be seen that the TALS-STI algorithm rapidly converges thanks to the knowledge of the non-impaired matrix \mathbf{S} that remains fixed during each iteration. Also, the number of iterations required for the convergence decreases as a function of the SNR. In the high SNR regime, the convergence of the proposed TALS-STI algorithm is no more sensitive to N , P and SNR values. When the SNR is higher than 20 dB, its convergence is quickly achieved within approximately 5 iterations.

In Fig. 9, we evaluate the overall computational complexity of the TALS-STI and HOSVD-STI algorithms using as metric the average runtime (in seconds). This metric takes into account the number of iterations for convergence, making it possible to compare the complexity between iterative and closed-form solutions. It can be seen that the runtime grows when the number of RIS elements N increases, confirming the results shown in Fig. 7. The runtime required by HOSVD-STI is not sensitive to the SNR since it is a closed-form algorithm. On the other hand, the runtime of the TALS-STI algorithm decreases with the SNR as it is an iterative algorithm, achieving performance close to HOSVD-STI algorithm in the high SNR regime thanks to its rapid convergence (Fig. 8).

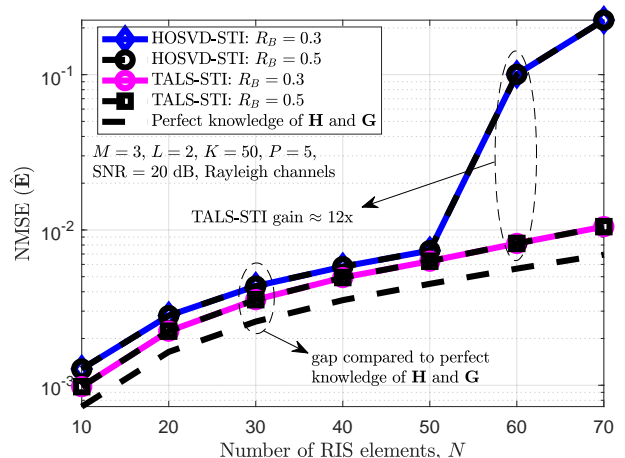
We can conclude that TALS-STI and HOSVD-STI algorithms outperform the method in [19] in terms of both channel estimation accuracy and overall computational complexity. This is because due to the RIS imperfections, the method in [19] does not estimate channels properly and has very slow convergence which directly increases its runtime. However, the TALS-STI can operate under more flexible choices for the number of time-blocks K for channel estimation compared to HOSVD-STI (see Fig. 10). From this, we can note that when the condition in (61) is not satisfied, the TALS-STI significantly outperforms the HOSVD-STI in terms of estimation accuracy. Therefore, a tradeoff between overall computational complexity, estimation performance and operation conditions for the proposed solutions can be observed. Thus, the TALS-STI may be attractive when more flexible



(a) NMSE of $\hat{\mathbf{H}}$ versus N .



(b) NMSE of $\hat{\mathbf{G}}$ versus N .



(c) NMSE of $\hat{\mathbf{E}}$ versus N .

Fig. 10: NMSE performance of the TALS-STI and HOSVD-STI algorithms versus the number of the RIS elements N for $M = 3$ transmit antennas, $L = 2$ receive antennas, $K = 50$ time-blocks, $P = 5$ frames, $\text{SNR} = 20 \text{ dB}$ and different impairments occurrence probability R_B assuming i.i.d. Rayleigh fading channels.

choices for the number of time-blocks for channel estimation K are required, while the HOSVD-STI is preferred specially

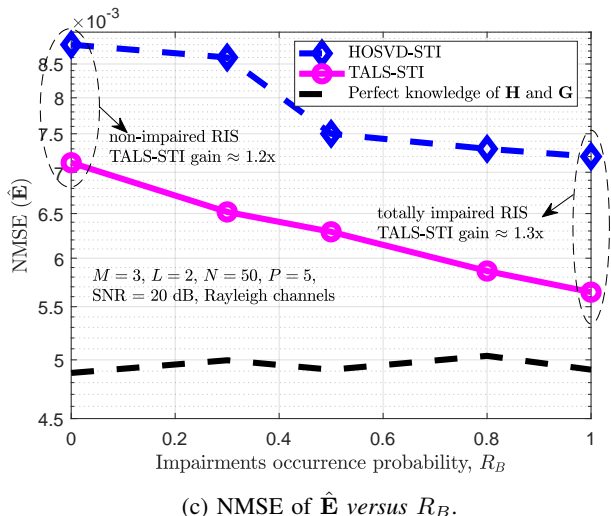
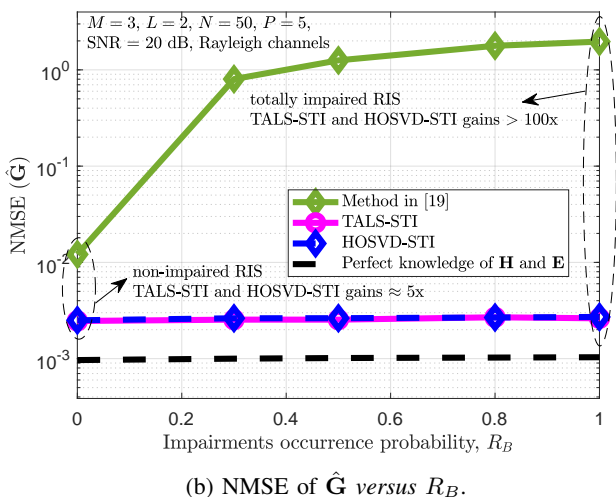
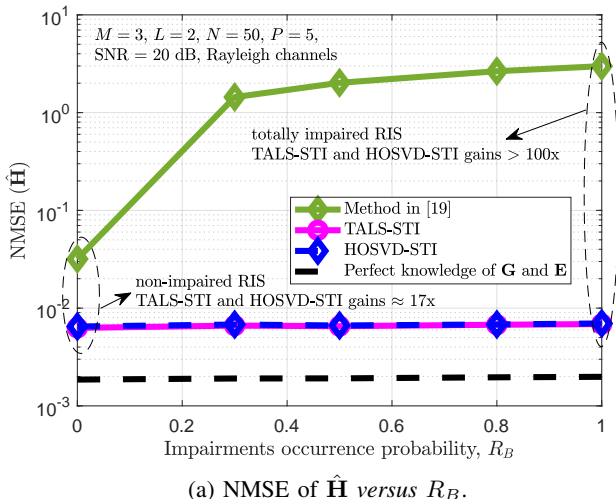


Fig. 11: NMSE performance of the TALS-STI and HOSVD-STI algorithms versus the impairments occurrence probability R_B for $M = 3$ transmit antennas, $L = 2$ receive antennas, $N = 50$ RIS elements, $K = 50$ time-blocks, $P = 5$ frames, SNR = 20 dB assuming i.i.d. Rayleigh fading channels.

when low processing delay is desired. We can also observe that the estimation performance degrades as the number of

RIS elements N increases, which is an expected result since the number of channel and imperfections coefficients to be estimated also increases with N .

In our last experiment, shown in Fig. 11, we evaluate the NMSE as a function of the impairments occurrence probability R_B . It can be seen that, in terms of channel estimation, for a broad range of parameter settings, our proposed approaches are not sensitive to the number of impaired elements at the RIS. This is because the imperfections matrix is estimated as an independent variable by both methods. However, in terms of imperfections estimation, the TALS-STI proves to be more accurate for all considered values of R_B . It is also important to note that the proposed TALS-STI and HOSVD-STI algorithms outperform the method in [19], even when ideal non-impaired RIS is assumed. However, the gains achieved by our methods become more evident in the challenging scenario, when the number of impaired elements at the RIS increases. In this case, the method of [19] is sensitive to R_B . Thus, if the number of impaired elements changes, it does not show a stable/predictable performance. This leads to the need for channel estimation correction and retransmissions. In contrast, our proposed methods are quite robust to R_B variation which simplifies the system design.

VI. CONCLUSION

We have proposed different efficient tensor-based algorithms for channel estimation in RIS-assisted MIMO systems, in which the RIS elements are affected by real-world imperfections. We resort to the multidimensional structure of the received signal to solve these non-idealized channel estimation problems by means of trilinear and quadrilinear PARAFAC models. The proposed TALS-LTI algorithm solves the problem when static imperfections are assumed. In a generalized way, we have formulated the TALS-STI and HOSVD-STI algorithms for the more challenging scenario in which the behavior of the RIS imperfections is non-static with respect to the channel coherence time. The TALS-LTI and TALS-STI algorithms are iterative solutions that relax the system design requirements, operating under more flexible choices for the training parameters. In contrast, the HOSVD-STI algorithm is a closed-form solution that has a lower computational complexity compared to the competing ALS-based solutions, while affording parallel processing. Simulation results illustrate the high estimation performance of the proposed tensor-based algorithms for different kinds of imperfections, channel models, and system configurations. The TALS-STI and HOSVD-STI algorithms present similar channel estimation performances. However, the TALS-STI is preferable for the imperfections detection in the low SNR regime and when more flexible choices for training parameters is required, while the HOSVD-STI is preferred when low processing delay is desired.

REFERENCES

- [1] P. R. B. Gomes, G. T. de Araújo, B. Sokal, A. L. F. de Almeida, B. Makki, and G. Fodor, "Tensor-based channel estimation for ris-assisted networks operating under imperfections," 2022. [Online]. Available: <https://arxiv.org/abs/2206.03557>
- [2] G. Forecast, "Cisco visual networking index: global mobile data traffic forecast update, 2017–2022," *Update*, vol. 2017, p. 2022, 2019.
- [3] ITU, "IMT traffic estimates for the years 2020 to 2030," ITU-R M, TR 2370-0, Jan. 2015, V.15.0.0.

- [4] S. Zhang, Q. Wu, S. Xu, and G. Y. Li, "Fundamental green tradeoffs: Progresses, challenges, and impacts on 5G networks," *IEEE Commun. Surveys Tuts.*, vol. 19, no. 1, pp. 33–56, Feb. 2016.
- [5] C. You, B. Zheng, and R. Zhang, "Channel estimation and passive beamforming for intelligent reflecting surface: Discrete phase shift and progressive refinement," *IEEE J. Sel. Areas Commun.*, vol. 38, no. 11, pp. 2604–2620, Jul. 2020.
- [6] Q. Wu, G. Y. Li, W. Chen, D. W. K. Ng, and R. Schober, "An overview of sustainable green 5G networks," *IEEE Wireless Communications*, vol. 24, no. 4, pp. 72–80, Aug. 2017.
- [7] G. Zhou, C. Pan, H. Ren, P. Popovski, and A. L. Swindlehurst, "Channel estimation for RIS-aided multiuser millimeter-wave systems," *IEEE Transactions on Signal Processing*, vol. 70, pp. 1478–1492, 2022.
- [8] M. Di Renzo, M. Debbah, D.-T. Phan-Huy, A. Zappone, M.-S. Alouini, C. Yuen, V. Sciancalepore, G. C. Alexandropoulos, J. Hoydis, H. Gacanin *et al.*, "Smart radio environments empowered by reconfigurable ai meta-surfaces: An idea whose time has come," *EURASIP Journal on Wireless Communications and Networking*, vol. 2019, no. 1, pp. 1–20, May. 2019.
- [9] Y.-C. Liang, R. Long, Q. Zhang, J. Chen, H. V. Cheng, and H. Guo, "Large intelligent surface/antennas (LISA): Making reflective radios smart," *Journal of Communications and Information Networks*, vol. 4, no. 2, pp. 40–50, Jun 2019.
- [10] M. Di Renzo, A. Zappone, M. Debbah, M.-S. Alouini, C. Yuen, J. de Rosny, and S. Tretyakov, "Smart radio environments empowered by reconfigurable intelligent surfaces: How it works, state of research, and the road ahead," *IEEE J. Sel. Areas Commun.*, vol. 38, no. 11, pp. 2450–2525, Jul. 2020.
- [11] N. Rajatheva, I. Atzeni, S. Bicaïs, E. Bjornson, A. Bourdoux, S. Buzzi, C. D'Andrea, J.-B. Dore, S. Erkucuk, M. Fuentes, K. Guan, Y. Hu, X. Huang, J. Hultkonen, J. M. Jornet, M. Katz, B. Makki, R. Nilsson, E. Panayirci, K. Rabie, N. Rajapaksha, M. Salehi, H. Sarieddeen, S. Shahabuddin, T. Svensson, O. Tervo, A. Tolli, Q. Wu, and W. Xu, "Scoring the terabit/s goal:broadband connectivity in 6G," Feb. 2021, arXiv:2008.07220v2.
- [12] E. Basar, M. Di Renzo, J. De Rosny, M. Debbah, M.-S. Alouini, and R. Zhang, "Wireless communications through reconfigurable intelligent surfaces," *IEEE access*, vol. 7, pp. 116 753–116 773, Jun. 2019.
- [13] Q. Wu and R. Zhang, "Towards smart and reconfigurable environment: Intelligent reflecting surface aided wireless network," *IEEE Communications Magazine*, vol. 58, no. 1, pp. 106–112, Nov. 2019.
- [14] H. Guo, B. Makki, M. Åström, M.-S. Alouini, and T. Svensson, "Dynamic blockage pre-avoidance using reconfigurable intelligent surfaces," 2022. [Online]. Available: <https://arxiv.org/abs/2201.06659>
- [15] 3GPP, "RWS-210300 NR repeaters and reconfigurable intelligent surface," in *3GPP TSG RAN Rel-18 workshop*. Electronic Meeting, June 28 - July 2, 2021.
- [16] A. Zappone, M. Di Renzo, F. Shams, X. Qian, and M. Debbah, "Overhead-aware design of reconfigurable intelligent surfaces in smart radio environments," *IEEE Trans. Wireless Commun.*, vol. 20, no. 1, pp. 126–141, Jan. 2021.
- [17] A. L. Swindlehurst, G. Zhou, R. Liu, C. Pan, and M. Li, "Channel estimation with reconfigurable intelligent surfaces—a general framework," *Proceedings of the IEEE*, pp. 1–27, 2022.
- [18] G. T. de Araújo, P. R. B. Gomes, A. L. F. de Almeida, G. Fodor, and B. Makki, "Semi-blind joint channel and symbol estimation in IRS-assisted multi-user mimo networks," *IEEE Wireless Commun. Lett.*, pp. 1–1, 2022.
- [19] G. T. de Araújo, A. L. de Almeida, and R. Boyer, "Channel estimation for intelligent reflecting surface assisted MIMO systems: A tensor modeling approach," *IEEE J. Sel. Topics Signal Process.*, vol. 15, no. 3, pp. 789–802, Feb. 2021.
- [20] Y. Yang, B. Zheng, S. Zhang, and R. Zhang, "Intelligent reflecting surface meets OFDM: Protocol design and rate maximization," *IEEE Trans. Commun.*, vol. 68, no. 7, pp. 4522–4535, Mar. 2020.
- [21] D. Mishra and H. Johansson, "Channel estimation and low-complexity beamforming design for passive intelligent surface assisted MISO wireless energy transfer," in *proc. ICASSP "2019"*, Brighton, UK, Apr.
- [22] Z.-Q. He and X. Yuan, "Cascaded channel estimation for large intelligent metasurface assisted massive MIMO," *IEEE Wireless Commun. Lett.*, vol. 9, no. 2, pp. 210–214, Feb. 2019.
- [23] A. Taha, M. Alrabeiah, and A. Alkhatib, "Enabling large intelligent surfaces with compressive sensing and deep learning," *IEEE Access*, vol. 9, pp. 44 304–44 321, Mar. 2021.
- [24] J. Chen, Y.-C. Liang, H. V. Cheng, and W. Yu, "Channel estimation for reconfigurable intelligent surface aided multi-user MIMO systems," Dec. 2019, arXiv:1912.03619v1 [eess.SP].
- [25] J. He, M. Leinonen, H. Wymeersch, and M. Juntti, "Channel estimation for RIS-aided mmwave MIMO systems," in *proc. GLOBECOM "2020"*, Taipei, Taiwan, Feb.
- [26] N. Sidiropoulos, G. Giannakis, and R. Bro, "Blind PARAFAC receivers for DS-CDMA systems," *IEEE Trans. Signal Process.*, vol. 48, no. 3, pp. 810–823, Mar. 2000.
- [27] H. Chen, F. Ahmad, S. Vorobyov, and F. Porikli, "Tensor decompositions in wireless communications and mimo radar," *IEEE J.Sel. Topics in Signal Process.*, vol. 15, no. 3, pp. 438–453, Feb. 2021.
- [28] N. D. Sidiropoulos, L. De Lathauwer, X. Fu, K. Huang, E. E. Papalexakis, and C. Faloutsos, "Tensor decomposition for signal processing and machine learning," *IEEE Trans. Signal Process.*, vol. 65, no. 13, pp. 3551–3582, Feb. 2017.
- [29] L. Wei, C. Huang, G. C. Alexandropoulos, and C. Yuen, "Parallel factor decomposition channel estimation in RIS-assisted multi-user MISO communication," in *proc. SAM "2020"*, Hangzhou, China, Jun.
- [30] G. T. de Araújo and A. L. de Almeida, "PARAFAC-based channel estimation for intelligent reflective surface assisted MIMO system," in *proc. SAM "2020"*, Hangzhou, China, Jun.
- [31] G. T. de Araújo and A. L. F. de Almeida, "Channel estimation for MIMO system assisted by intelligent reflective surface," in *proc. SBRt "2020"*, Santa Catarina, Brazil, Nov.
- [32] X. Qian, M. Di Renzo, J. Liu, A. Kammoun, and M.-S. Alouini, "Beamforming through reconfigurable intelligent surfaces in single-user MIMO systems: SNR distribution and scaling laws in the presence of channel fading and phase noise," *IEEE Wireless Commun. Lett.*, vol. 10, no. 1, pp. 77–81, Sep. 2021.
- [33] M.-A. Badiu and J. P. Coon, "Communication through a large reflecting surface with phase errors," *IEEE Wireless Commun. Lett.*, vol. 9, no. 2, pp. 184–188, Feb. 2020.
- [34] S. Zhou, W. Xu, K. Wang, M. Di Renzo, and M.-S. Alouini, "Spectral and energy efficiency of IRS-assisted MISO communication with hardware impairments," *IEEE wireless commun. lett.*, vol. 9, no. 9, pp. 1366–1369, Sep. 2020.
- [35] K. Zhi, C. Pan, H. Ren, and K. Wang, "Uplink achievable rate of intelligent reflecting surface-aided millimeter-wave communications with low-resolution ADC and phase noise," *IEEE Wireless Commun. Lett.*, vol. 10, no. 3, pp. 654–658, Mar. 2021.
- [36] B. Li, Z. Zhang, Z. Hu, and Y. Chen, "Joint array diagnosis and channel estimation for RIS-aided mmwave MIMO system," *IEEE Access*, vol. 8, pp. 193 992–194 006, Oct. 2020.
- [37] B. Li, Z. Zhang, and Z. Hu, "Channel estimation for reconfigurable intelligent surface-assisted multiuser mmwave MIMO system in the presence of array blockage," *Transactions on Emerging Telecommunications Technologies*, vol. 32, no. 11, p. e4322, Jun. 2021.
- [38] T. G. Kolda and B. W. Bader, "Tensor decompositions and applications," *SIAM review*, vol. 51, no. 3, pp. 455–500, Aug. 2009.
- [39] L. De Lathauwer, B. De Moor, and J. Vandewalle, "A multilinear singular value decomposition," *SIAM Journal on Matrix Analysis and Applications*, vol. 21, no. 4, pp. 1253–1278, Apr. 2000.
- [40] S. Abeywickrama, R. Zhang, Q. Wu, and C. Yuen, "Intelligent reflecting surface: Practical phase shift model and beamforming optimization," *IEEE Trans. Commun.*, vol. 68, no. 9, pp. 5849–5863, Sep. 2020.
- [41] Z. Yigit, E. Basar, and I. Altunbas, "Low complexity adaptation for reconfigurable intelligent surface-based MIMO systems," *IEEE Commun. Lett.*, vol. 24, no. 12, pp. 2946–2950, Dec. 2020.
- [42] B. Sokal, P. R. B. Gomes, A. L. F. de Almeida, B. Makki, and G. Fodor, "IRS phase-shift feedback overhead-aware model based on rank-one tensor approximation," 2022. [Online]. Available: <https://arxiv.org/abs/2205.12024>
- [43] —, "Reducing the control overhead of intelligent reconfigurable surfaces via a tensor-based low-rank factorization approach," 2022. [Online]. Available: <https://arxiv.org/abs/2206.05341>
- [44] R. Bro, "Multi-way analysis in the food industry—models, algorithms, and applications," in *MRI, EPG and EMA*, Proc ICSP 2000. Citeseer, 1998.
- [45] X.-F. Gong and Q.-H. Lin, "Spatially constrained parallel factor analysis for semi-blind beamforming," in *2011 Seventh International Conference on Natural Computation*, vol. 1. IEEE, 2011, pp. 416–420.
- [46] Z. Wang, C. Cai, F. Wen, and D. Huang, "A quadrilinear decomposition method for direction estimation in bistatic MIMO radar," *IEEE Access*, vol. 6, pp. 13 766–13 772, Mar. 2018.
- [47] T. L. Jensen and E. De Carvalho, "An optimal channel estimation scheme for intelligent reflecting surfaces based on a minimum variance unbiased estimator," in *proc. ICASSP "2020"*, Barcelona, Spain, May.